PAHs as tracers of the molecular gas in star-forming galaxies

I Cortzen, J Garrett, G Magdis, D Rigopoulou, F Valentino, M Pereira-Santaella, F Combes, A Alonso-Herrero, S Toft, E Daddi, et al.

Monthly Notices
of the
ROYAL ASTRONOMICAL SOCIETY

MNRAS **482,** 1618–1633 (2019)
Advance Access publication 2018 October 13

doi:10.1093/mnras/sty2777

PAHs as tracers of the molecular gas in star-forming galaxies

I. Cortzen [1,2★] J. Garrett,[3] G. Magdis,[1,2★] D. Rigopoulou,[3] F. Valentino [1,2] M. Pereira-Santaella [3] F. Combes,[4] A. Alonso-Herrero,[5] S. Toft,[1,2] E. Daddi [6] D. Elbaz,[6] C. Gómez-Guijarro [1,2] M. Stockmann,[1,2] J. Huang[7] and C. Kramer[8]

[1]*Cosmic Dawn Center (DAWN), Niels Bohr Institute, University of Copenhagen, Juliane Maries Vej 30, DK-2100 Copenhagen Ø, Denmark; DTU-Space, Technical University of Denmark, Elektrovej 327, DK-2800 Kgs. Lyngby, Denmark*
[2]*Dark Cosmology Centre, Niels Bohr Institute, University of Copenhagen, Juliane Maries Vej 30, DK-2100 Copenhagen Ø, Denmark*
[3]*Department of Physics, University of Oxford, Keble Road, Oxford OX1 3RH, UK*
[4]*Observatoire de Paris, LERMA, College de France, DNRS, PSL, Sorbonne Univ. UPMC, F-75014 Paris, France*
[5]*Centro de Astrobiología (CAB, CSIC-INTA), ESAC Campus, E-28692 Villanueva de la Cañada, Madrid, Spain*
[6]*CEA Saclay, Laboratoire AIM-CNRS-Université Paris Diderot, Irfu/SAp, Orme des Merisiers, F-91191 Gif-sur Yvette, France*
[7]*National Astronomical Observatories of China, Chinese Academy of Sciences, 100012 Beijing, PR China*
[8]*Instituto de Radioastronomía Milimétrica, Av. Divina Pastora 7, Núcleo Central, E-18012 Granada, Spain*

Accepted 2018 October 9. Received 2018 October 2; in original form 2018 May 14

ABSTRACT

We combine new CO(1–0) line observations of 24 intermediate redshift galaxies ($0.03 < z < 0.28$) along with literature data of galaxies at $0 < z < 4$ to explore scaling relations between the dust and gas content using polycyclic aromatic hydrocarbon (PAH) 6.2 μm ($L_{6.2}$), CO ($L'_{\rm CO}$), and infrared ($L_{\rm IR}$) luminosities for a wide range of redshifts and physical environments. Our analysis confirms the existence of a universal $L_{6.2}$–$L'_{\rm CO}$ correlation followed by normal star-forming galaxies (SFGs) and starbursts (SBs) at all redshifts. This relation is also followed by local ultraluminous infrared galaxies that appear as outliers in the $L_{6.2}$–$L_{\rm IR}$ and $L_{\rm IR}$–$L'_{\rm CO}$ relations defined by normal SFGs. The emerging tight ($\sigma \approx 0.26$ dex) and linear ($\alpha = 1.03$) relation between $L_{6.2}$ and $L'_{\rm CO}$ indicates a $L_{6.2}$ to molecular gas ($M_{\rm H_2}$) conversion factor of $\alpha_{6.2} = M_{\rm H_2}/L_{6.2} = (2.7 \pm 1.3) \times \alpha_{\rm CO}$, where $\alpha_{\rm CO}$ is the $L'_{\rm CO}$ to $M_{\rm H_2}$ conversion factor. We also find that on galaxy integrated scales, PAH emission is better correlated with cold rather than with warm dust emission, suggesting that PAHs are associated with the diffuse cold dust, which is another proxy for $M_{\rm H_2}$. Focusing on normal SFGs among our sample, we employ the dust continuum emission to derive $M_{\rm H_2}$ estimates and find a constant $M_{\rm H_2}/L_{6.2}$ ratio of $\alpha_{6.2} = 12.3\ {\rm M_\odot/L_\odot}$($\sigma \approx 0.3$ dex). This ratio is in excellent agreement with the $L'_{\rm CO}$-based $M_{\rm H_2}/L_{6.2}$ values for $\alpha_{\rm CO} = 4.5\ {\rm M_\odot/(K\,km\,s^{-1}\,pc^2)}$ which is typical of normal SFGs. We propose that the presented $L_{6.2}$–$L'_{\rm CO}$ and $L_{6.2}$–$M_{\rm H_2}$ relations will serve as useful tools for the determination of the physical properties of high-z SFGs, for which PAH emission will be routinely detected by the *James Webb Space Telescope*.

Key words: galaxies: active – galaxies: evolution – galaxies: ISM – galaxies: star formation.

1 INTRODUCTION

The mid-infrared (MIR; 3–25 μm) spectrum of star-forming galaxies (SFGs) is dominated by strong emission features generally attributed to polycyclic aromatic hydrocarbons (PAHs) (Sellgren 1984; Puget & Leger 1989; Helou et al. 2001; Pahre et al. 2004; Tielens 2008). The extensive observations of PAH emission in galaxies at both low and high redshifts from either the *Infrared Space Observatory* (Genzel et al. 1998; Lutz et al. 1998; Rigopoulou et al. 1999) or InfraRed Spectrograph (IRS) on the *Spitzer Space Telescope* (Armus et al. 2007; Houck et al. 2007; Spoon et al. 2007; Valiante et al. 2007; Yan et al. 2007; Farrah et al. 2008; Sajina et al. 2008; Murphy et al. 2009; O'Dowd et al. 2009; Veilleux et al. 2009; Fadda et al. 2010; Pereira-Santaella et al. 2010; Riechers et al. 2014) indicate that they are ubiquitous and an important tracer of the interstellar medium (ISM). PAH molecules, which are stochastically heated by optical and UV photons, dominate the photoelectric heating rates of the neutral gas and the ionization balance within molecular clouds (Bakes & Tielens 1994). The emission arising from these abundant species can contribute up to 20 per cent of the total infrared (IR) emission in galaxies depending on the physical conditions (Smith

★ E-mail: cortzen@nbi.ku.dk (IC); georgios.magdis@nbi.ku.dk (GM)

et al. 2007; Dale et al. 2009). Hard UV photon fields are thought to destroy, fragment, or ionize the PAH molecules (Boulanger et al. 1988, 1990; Helou, Ryter & Soifer 1991; Pety et al. 2005), whereas low-metallicity systems reveal suppressed PAH emission (Engelbracht et al. 2005; Hunt et al. 2010). The origin of PAHs has been widely discussed in previous studies suggesting that they can be formed in either the envelopes or outflows of carbon-rich AGB stars (Latter 1991; Cherchneff, Barker & Tielens 1992), massive red supergiants (Melbourne & Boyer 2013), or in the ISM itself (Tielens et al. 1987; Puget & Leger 1989; Herbst 1991; Sandstrom et al. 2010, 2012, 2013).

In the local Universe, PAH emission and its link to star formation has been thoroughly studied within the Milky Way and in nearby galaxies through various star formation tracers: individual observations of H II regions revealed that the PAH emission is found in shell-like structures around the star-forming regions (Churchwell et al. 2006; Rho et al. 2006), with a notable decrease of their strength within the H II regions (Helou et al. 2004; Calzetti et al. 2005, 2007; Lebouteiller et al. 2007; Povich et al. 2007; Thilker et al. 2007). On larger scales, previous studies have found that SFGs at both low and high redshifts follow a linear relation between the integrated luminosity of the PAH 6.2 μm feature ($L_{6.2}$) and the total infrared luminosity ($L_{\rm IR}$), where the latter is the sum of the re-radiated emission from dust grains and a commonly used tracer for the star formation rate (SFR) (Schmidt 1959; Kennicutt 1998; Roussel et al. 2001; Förster Schreiber et al. 2004; Armus et al. 2007; Huang et al. 2009; Menéndez-Delmestre et al. 2009; Rujopakarn et al. 2013). PAH emission has also been observed in both ultraluminous infrared galaxies (ULIRGs; $L_{\rm IR} > 10^{12}$ L$_\odot$) (Genzel et al. 1998; Armus et al. 2007; Desai et al. 2007) and galaxies with the presence of an active galactic nucleus (AGN) (Moorwood 1986; Roche et al. 1991; Weedman et al. 2005; Smith et al. 2007; Alonso-Herrero et al. 2016; Jensen et al. 2017; Kirkpatrick et al. 2017), however with an on average smaller PAH equivalent. As such the equivalent width of the PAH features can be used to distinguish between AGN and/or strong starbursting galaxies from normal, star-formation dominated systems (Laurent et al. 2000; Brandl et al. 2006; Sajina et al. 2007; Spoon et al. 2007; Pope et al. 2008; Shipley et al. 2013; Esquej et al. 2014). For AGN-dominated galaxies, the total IR emission may also arise from dust heated by the AGN rather than star formation activity, especially in wavelengths shorter than the peak of the FIR SED (e.g. Smith et al. 2007; Wu et al. 2010; Mullaney et al. 2013; Shipley et al. 2013). Lower $L_{\rm PAH}/L_{\rm IR}$ ratios have previously been observed in AGN-dominated sources with respect to SFGs (Armus et al. 2007; Valiante et al. 2007; Sajina et al. 2008) suggesting that PAHs at 6.2, 7.7, and 8.6 μm are suppressed due to the presence of an AGN (Diamond-Stanic & Rieke 2010). Interestingly though, recent works in the local Universe report strong PAH 11.3 μm emission from the nuclear regions of Seyfert galaxies and QSOs (Hönig et al. 2010; Alonso-Herrero et al. 2014; Esquej et al. 2014; Alonso-Herrero et al. 2016), indicating that PAH molecules could be excited, rather than destroyed, by the AGN itself (Jensen et al. 2017).

A similar trend to $L_{\rm PAH}$–$L_{\rm IR}$ has been observed between the luminosity of the CO(1–0) transition line ($L'_{\rm CO}$), a common tracer of molecular gas, and the $L_{\rm IR}$. The majority of SFGs follow a tight relation between the SFR (traced by $L_{\rm IR}$) and the cold molecular gas (traced by $L'_{\rm CO}$) or the total gas content ($M_{\rm gas}$), which is known as the Kennicutt–Schmidt (KS) law spanning a large dynamical range (Schmidt 1959; Kennicutt 1998). Similar to the $L_{\rm IR}$–$L_{6.2}$ relation starbursting systems also appear as outliers in $L_{\rm IR}$–$L'_{\rm CO}$ relation, exhibiting an enhanced star formation efficiency (SFE $= L_{\rm IR}/L'_{\rm CO}$) possibly driven by a major merger event, as supported by observations of local ULIRGs and a fraction of submillimeter galaxies (SMGs) at high redshift (Rigopoulou et al. 1999; Pope et al. 2013). The weaker PAH and CO emission (for a fixed $L_{\rm IR}$) in these star-formation dominated galaxies can be explained by compact star-forming regions and high SFEs due to a larger fraction of dense molecular gas (Tacconi et al. 2008; Daddi et al. 2010a,b; Díaz-Santos et al. 2011; Pope et al. 2013; Kirkpatrick et al. 2014). To this direction, Elbaz et al. (2011) found that the IR8 $= L_{\rm IR}/L_8$[1] ratio can be used to separate normal SFGs with extended star-formation activity that also lay predominantly on the so-called 'main-sequence' (MS) of galaxies (Elbaz et al. 2007; Magdis et al. 2010; Schreiber et al. 2015) from compact starbursts (SBs). Also, for star-formation dominated galaxies, Magdis et al. (2013) reported that IR8 variations are driven mainly by the strength of the PAH features rather than continuum variations, again indicative of more compact star formation for sources with weaker PAH features.

Finally, several studies have revealed a connection between PAHs and the molecular gas ($M_{\rm H_2}$) as traced by CO emission. Analyses of the observed radial profiles of PAH and CO emission in local galaxies indicate that PAHs can be used as a proxy for the molecular ISM in galaxies (Regan et al. 2006). The link between PAHs and molecular gas is further supported not only by the observed correlations between PAHs and CO emission on galaxy integrated scales (Pope et al. 2013), but also between PAHs and cold dust emission at ≥160 μm (e.g. Haas, Klaas & Bianchi 2002; Bendo et al. 2008; Jones et al. 2015).

In this work, we further explore the connection between the PAHs and the molecular gas of galaxies, with new single-dish CO(1–0) line observations of 34 IR-bright PAH-emitting SFGs across the MS selected from the 5MUSES survey (Wu et al. 2010), increasing the existing sample of PAH-, IR-, and CO-detected galaxies at intermediate redshifts ($0.03 < z < 0.28$) by a factor of 2.4 (Section 2). We complement our sample with existing CO(1–0) and PAH observations from the literature in order to determine the scatter of the scaling relations between IR, PAH, and CO data spanning two orders of magnitude in luminosity and covering a broad range of redshifts ($0 < z < 4$). In Section 3.1, we present the $L_{6.2}$–$L_{\rm IR}$ for normal SFGs and identify local ULIRGs and high-z SBs as clear outliers characterized by lower $L_{6.2}/L_{\rm IR}$ ratios. In Section 3.2, we show that these outliers also exhibit lower $L'_{\rm CO}/L_{\rm IR}$ ratios compared to the $L'_{\rm CO}$–$L_{\rm IR}$ relation defined by the general population of normal galaxies. On the other hand, in Section 3.3 we present a universal $L_{6.2}$–$L'_{\rm CO}$ relation followed by both normal SFGs and SBs at all redshifts. This, along with the strong correlation between the PAH and cold dust emission ($\lambda \geq 160$ μm) presented in Section 3.4, motivates us to explore PAHs as a proxy for the molecular gas in Section 3.5.

Throughout this paper we adopt a standard cosmology with $H_0 = 70\,{\rm km\,s^{-1}\,Mpc^{-1}}$, $\Omega_{\rm M} = 0.30$, and $\Omega_\Lambda = 0.70$.

2 DATA SAMPLE

We have selected 34 star-forming targets from the 5 mJy Unbiased *Spitzer* Extragalactic Survey (5MUSES; Wu et al. 2010) in order to examine the gas and ISM properties of star-formation dominated galaxies at intermediate redshift ($0.03 < z < 0.28$) by detecting

[1] L_8 is the monochromatic luminosity at rest frame 8 μm as traced by the IRAC 8.0 μm band, which covers both the PAH 6.2, 7.7, and 8.6 μm complex at low redshift.

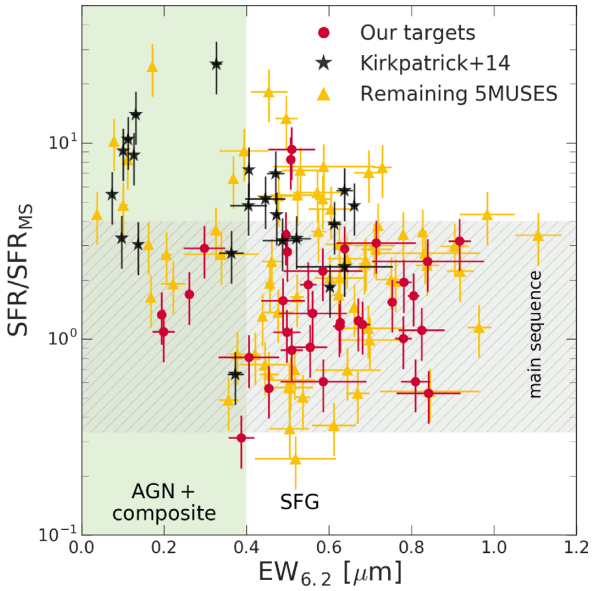

Figure 1. The equivalent width of the PAH 6.2 μm feature ($EW_{6.2}$) versus offset from the MS (grey shaded region). The red points depict galaxies selected for CO(1–0) line observations presented in this study. Previously CO-detected 5MUSES galaxies from Kirkpatrick et al. (2014) are shown in black, whereas the rest of the 5MUSES sources are shown in yellow. Galaxies with $EW_{6.2} \leq 0.4$ μm are classified as AGN-dominated or composite sources (green region).

CO(1–0) emission and using existing observations. 5MUSES is a 24 μm flux-limited ($f_{24\mu m} > 5$ mJy) spectroscopic survey with *Spitzer* IRS, containing 330 galaxies with $L_{IR} \sim 10^{10}$–10^{12} $L_\odot$ located in the SWIRE (Lonsdale et al. 2003) and Extragalactic First Look Survey (XFLS) fields (Fadda et al. 2006). The sample fills out the gap between local SFGs (Kennicutt et al. 2003; Smith et al. 2007; Dale et al. 2009), low-z ULIRGs (Armus et al. 2007; Desai et al. 2007; Veilleux et al. 2009), and more distant galaxies with available spectroscopy data (Houck et al. 2005; Yan et al. 2007). In addition, the full sample has *Spitzer* Infrared Array Camera observations (IRAC; Fazio et al. 2004) at 3.6–8 μm and Multiband Imaging Photometer (MIPS; Rieke et al. 2004) at 70–160 μm (Wu et al. 2010), where 90 per cent and 54 per cent of the galaxies are detected at 70 and 160 μm, respectively.

From the 5MUSES sample, 280 galaxies have spectroscopically confirmed redshifts with low-resolution ($R = 64$–128) MIR spectra which were collected using the short-low (SL: 5.5–14.5 μm) and long-low (LL: 14–35 μm) spectral modules of the *Spitzer* IRS (Houck et al. 2005) as described in Wu et al. (2010). In addition to *Spitzer* IRAC, MIPS, and IRS observations, a subsample of 188 galaxies (with spectroscopically confirmed redshifts) have FIR photometric coverage at 250, 350, and 500 μm obtained with the *Herschel Space Observatory* (Griffin et al. 2010) through SPIRE observations as part of the *Herschel* Multi-tiered Extragalactic Survey (HerMES; Oliver et al. 2010, 2012). Out of the 188 sources, a flux density limit of $S_\nu > 15$ mJy in the *Herschel* SPIRE bands yields a detection for 154 (82 per cent), 108 (57 per cent), and 50 (27 per cent) sources at 250 μm, 350 μm, and 500 μm, respectively (Magdis et al. 2013). Stellar masses of the full 5MUSES sample have been estimated by Shi et al. (2011) using the Bruzual & Charlot (2003) population synthesis model to fit optical and IR photometry assuming a Chabrier (2003) IMF.

In Fig. 1, we present the equivalent width of the PAH 6.2 μm ($EW_{6.2}$) versus distance from the MS for the full 5MUSES sample. The offset from the MS, $SFR/SFR_{MS}(z, M_*)$, is determined by adopting equation 9 in Schreiber et al. (2015) after converting our stellar masses from a Chabrier (2003) IMF to a Salpeter (1955) IMF using $M_*^S = 1.70 \times M_*^C$ (Speagle et al. 2014). SFRs are derived using L_{IR} estimates (Section 2.3). We use optical spectroscopy and/or the $EW_{6.2}$ to identify AGN-dominated sources in the sample. In the absence of optical spectroscopy, we classify sources with $EW_{6.2} \leq 0.4$ μm as AGN and composite sources (see Wu et al. 2010; Magdis et al. 2013, for a detailed AGN characterization of the 5MUSES sample). Since we aim at examining the ISM properties of normal galaxies at intermediate redshifts, we primarily selected targets with $EW_{6.2} > 0.4$ μm across the MS ($SFR/SFR_{MS} < 4$) for follow-up CO(1–0) line observations. Moreover, all of our targets have *Spitzer* and *Herschel* observations, $L_{IR} = 10^{9.2}$–$10^{11.8}$ $L_\odot$, and stellar masses of $\langle M_* \rangle = 10^{10}$ $M_\odot$.

2.1 New CO(1–0) line observations

The single-dish observations were carried out with the IRAM 30 m telescope at Pico Veleta, Spain, in 2015 July, 2015 June, and 2016 September. All galaxies were observed at 3 mm using the spectral line receiver band E0 of EMIR with WILMA as backends in order to observe the CO(1–0) emission line. The receiver was tuned to the expected frequency of the targets (in the range 95 GHz $< \nu <$ 107 GHz) and the wobbler switching mode was used. We spent one to eight hours on each galaxy. During observations the pointing of the telescope was checked every two hours using a bright nearby source. The velocity-integrated CO line intensities were converted from antenna temperature scale (T_a^*) to Jy using $S/T_a^* = 6.2$ Jy K^{-1}. The CO(1–0) line luminosities were estimated in units of [K km s^{-1} pc^2] using the following equation from Solomon & Vanden Bout (2005):

$$L'_{CO} = 3.25 \times 10^7 S_{CO}\Delta v\, \nu_{obs}^{-2}\, D_L^2 (1+z)^3, \quad (1)$$

where $S_{CO}\Delta v$ [Jy km s^{-1}] is the velocity integrated flux, ν_{obs} [GHz] is the observed CO(1–0) frequency, and D_L [Mpc] is the luminosity distance.

Spectra were reduced using the CLASS/GILDAS[2] software, where each galaxy spectrum was averaged and smoothed to a velocity resolution of 70–100 km s^{-1}. Linear baselines were assumed for all targets. The spectra of galaxies with detected CO(1–0) line emission are shown in Fig. 2. A detected CO line is considered when the integrated signal is above 3σ. We detect significant CO line emission in 24 galaxies, whereas upper limits are determined for the remaining targets assuming a CO(1–0) line width of 300 km s^{-1}. The CO luminosities and the observed properties of each galaxy from our observing runs are listed in Table 1.

2.2 Literature data

To expand our data sample, we include published observations of galaxies at all redshifts with both CO, IR, and PAH detection from the literature. General properties of the data compilation are listed in Table 2.

2.2.1 5MUSES galaxies

In a recent study, Kirkpatrick et al. (2014) carried out CO(1–0) line observations of 24 intermediate redshift galaxies ($z = 0.04$–0.36), also selected from the 5MUSES sample, with the Redshift

[2]http://www.iram.fr/IRAMFR/GILDAS

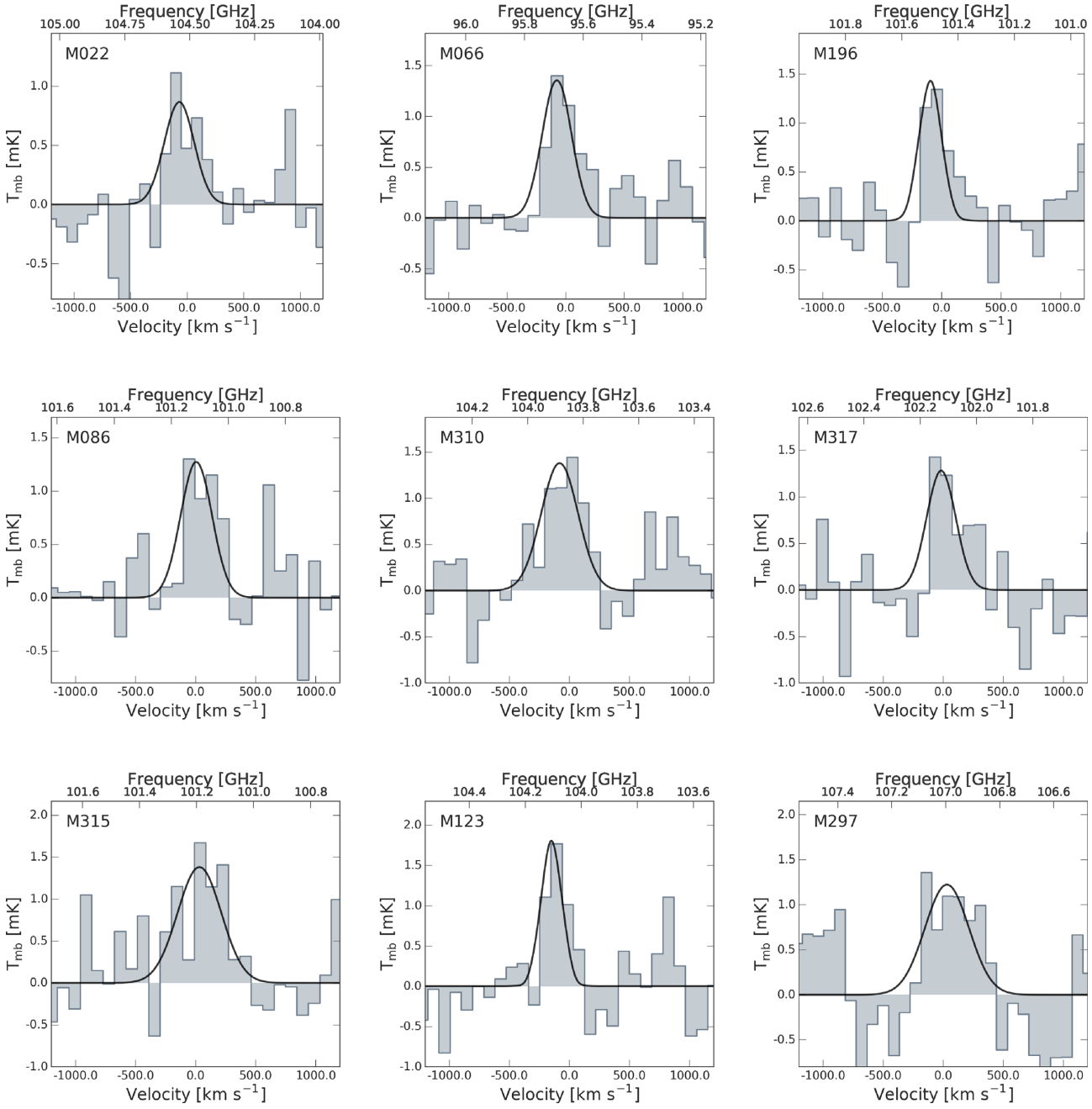

Figure 2. CO(1–0) spectra with antenna temperature [mK] as a function of velocity [km s^{-1}] of CO-detected 5MUSES galaxies followed-up with IRAM/EMIR. All spectra are smoothed to a velocity resolution of ∼70 km s^{-1}. A line is considered detected if the integrated signal is above 3σ. The black line shows the best-fitting Gaussian profile to the observed CO line.

Search Receiver on the Large Millimetre Telescope. Their sample covers a broader range of L_{IR} ($10^{10.4}$–$10^{12.1}$ $L_{\odot}$) and $EW_{6.2}$ (0.07–0.70 μm) as opposed to our targets. They detected CO(1–0) emission in 17 of the 24 sources which we combine with our sample for the analysis (14 of these have 3σ PAH 6.2 μm detection). For consistency, we derive CO line luminosities using the velocity-integrated line flux reported in Kirkpatrick et al. (2014). The final sample of intermediate redshift galaxies with both CO and PAH 6.2 μm detections in our study consists of 36 targets, all drawn from the 5MUSES compilation, of which 24 are from our new IRAM survey and 14 from Kirkpatrick et al. (2014).

2.2.2 *SINGS*

The *Spitzer* Infrared Nearby Galaxy Survey (SINGS; Kennicutt et al. 2003) is an imaging and low-resolution ($R \sim 50$–100) spectroscopic survey of 75 local galaxies with 5–38 μm spectral mapping with *Spitzer* IRS. The low-resolution 5–15 μm spectral map (55 arcsec × 34 arcsec) is centred on the nucleus of each galaxy. From the SINGS sample, Smith et al. (2007) selected 59 galaxies with

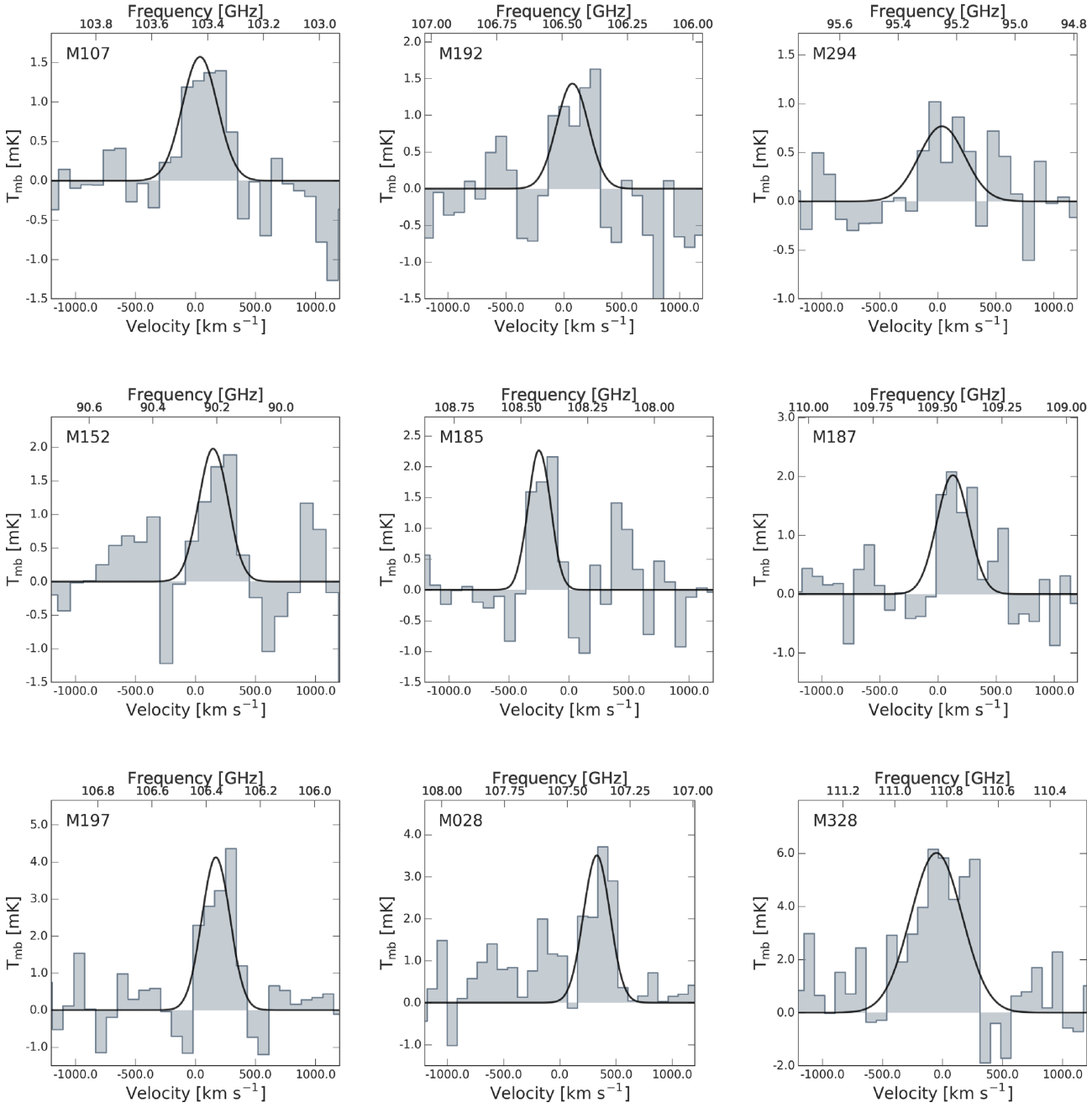

Figure 2 *–Continued*

spectral coverage between 5 and 38 μm from both SL and LL in order to detect PAH emission within the central regions of each galaxy. PAH features were derived using PAHFIT (Smith et al. 2007) and fitted with Drude profiles. A subsample of 57 SINGS galaxies have both PAH emission and FIR coverage based on *Herschel* PACS and SPIRE observations as presented in Dale et al. (2012).

From the SINGS survey, Wilson et al. (2012) selected 47 galaxies (NGLS: Nearby Galaxies Legacy Survey) to carry out CO(3–2) line observations with the James Clerk Maxwell Telescope. To correct the CO(3–2) emission to CO(1–0) we adopt a CO(3–2)/CO(1–0) line ratio of $r_{32/10} = 0.18 \pm 0.02$ based on a comparison study by Wilson et al. (2012). They estimate an average CO(3–2) and CO(1–0) line ratio using 11 nearby galaxies from the NGLS sample that overlap with CO(2–1) observations carried out by Kuno et al. (2007). We apply an aperture correction ($f_{\rm TIR}$) listed in Smith et al. (2007) to the IR and CO(1–0) luminosities and increase the uncertainties of the aperture-corrected luminosities by a factor of 2 in order to compare these with the PAH emission arising from the central part of the galaxy.

Given the different physical scales probed by the available PAH, CO, and dust emission observations of the SINGS galaxies, we choose to exclude them from our statistical analysis to avoid biases in our regression models due to possible systematics and uncertainties introduced by the aperture corrections. However, since the SINGS sample consists of representative, normal PAH emitting SFGs in the local Universe, for the sake of completeness we

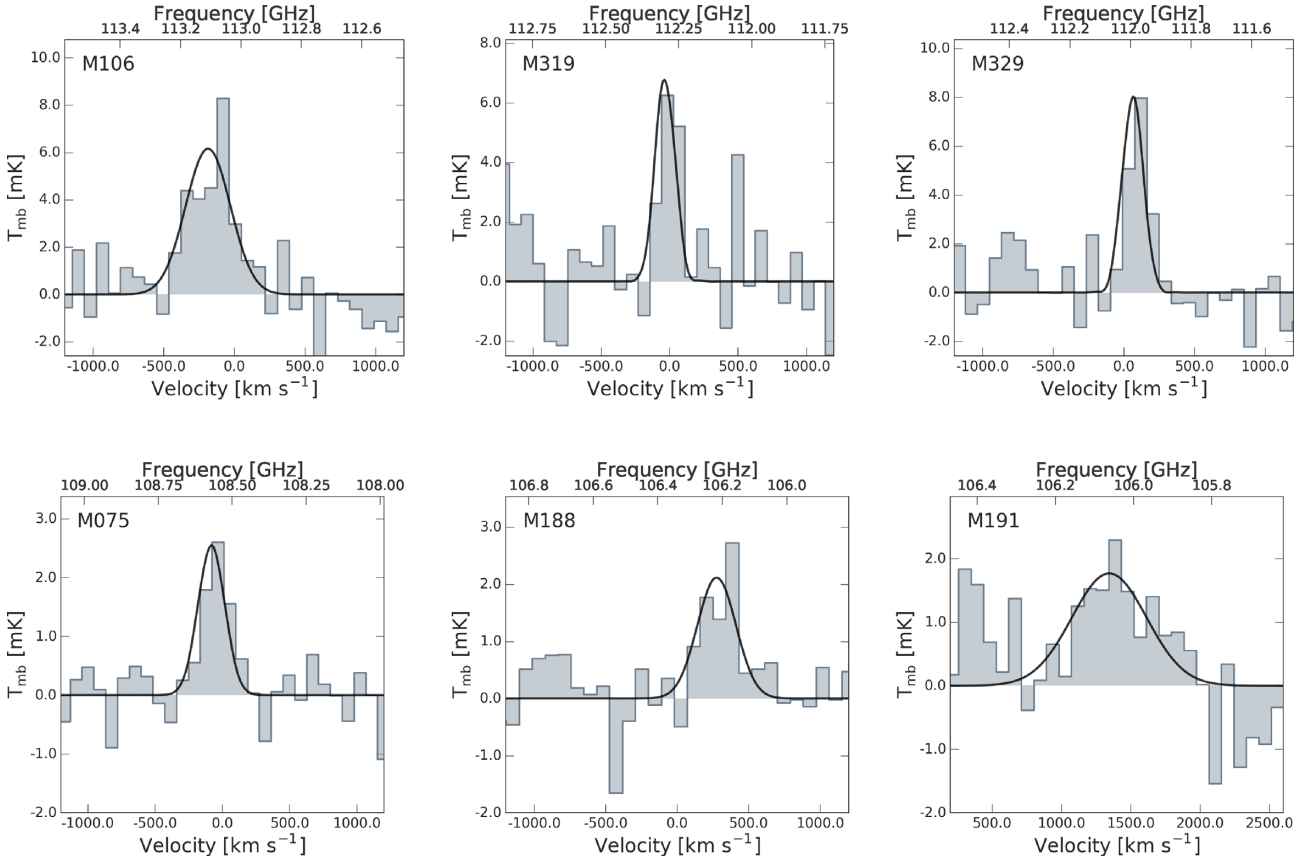

Figure 2 *–Continued*

choose to overplot them in the various luminosity scaling relations presented in this study.

2.2.3 *Local ULIRGs and high-z galaxies*

Pope et al. (2013) carried out CO(2–1) observations using IRAM PdBI and *Spitzer* MIR spectroscopy of six 70 μm selected galaxies from the *Spitzer* Far-Infrared Deep Extragalactic Legacy survey (Dickinson & FIDEL Team 2007) of GOODS-N with optical spectroscopic redshift at $z = 1$–1.5. The sample has *Spitzer* IRS observations and photometric coverage from *Spitzer* MIPS (24 and 70 μm) and *Herschel* PACS (100 and 160 μm) and SPIRE (250, 350, and 500 μm) observations from the GOODS-*Herschel* survey (Elbaz et al. 2011). As in Pope et al. (2013), we complement our sample with galaxies from the literature containing detected CO and PAH emission at all redshifts. These include 12 high-z galaxies (SMGs, BzKs, and 70 μm selected galaxies) from various studies at $1.1 < z < 4.1$ (Frayer et al. 2008; Pope et al. 2008; Aravena et al. 2010; Carilli et al. 2010; Casey et al. 2011; Ivison et al. 2011; Magnelli et al. 2012; Bothwell et al. 2013; Riechers et al. 2013). Stellar masses from Pope et al. (2013) are available for the 70 μm selected galaxies. Based on the offset from the MS, we classify the 70 μm as high-z SFGs galaxies whereas the remaining galaxies at $z > 1$ are labelled as SMGs. Similarly, we include the 24 μm selected sample ($S_{24} > 0.9$ mJy) of nine $z \sim 1$–2 ULIRGs in the *Spitzer* XFLS field with CO(2–1) or CO(3–2) observations from Yan et al. (2010) that also has existing *Spitzer* MIR spectra published in Yan et al. (2007) and Sajina et al. (2007).

For galaxies with only high-J CO line observations, we convert the CO luminosities to $L'_{\rm CO}$ by adopting the conversion factors listed in Bothwell et al. (2013, $r_{21/10} = 0.84 \pm 0.13$, $r_{32/10} = 0.52 \pm 0.09$, $r_{43/10} = 0.41 \pm 0.07$). At lower redshift, we also include 13 local ULIRGs with *Spitzer* IRS MIR spectra from Armus et al. (2007) and Desai et al. (2007) with existing CO observations and IR luminosities (Sanders, Scoville & Soifer 1991; Solomon et al. 1997; Kim, Veilleux & Sanders 1998; Farrah et al. 2003; Gao & Solomon 2004; Chung et al. 2009). The CO, IR, and PAH luminosities of the literature compilation are available in the online version (See Table 4).

2.3 Derivation of MIR and FIR dust properties

We combine the existing multiwavelength photometry from *Spitzer* (MIPS: 24, 160 μm) and *Herschel* (SPIRE: 250, 350, 500 μm) in order to estimate IR luminosities and dust masses ($M_{\rm dust}$) by modelling the FIR part of the spectral energy distribution (SED) for each galaxy in the 5MUSES sample. We use silicate–graphite–PAH models from Draine & Li (2007) (DL07) including diffuse ISM and photodissociation region (PDR) components. The best-fitting parameters and results are listed in the online version (see Table 3). $L_{\rm IR}$ is derived by integrating the SED model between rest frame 8–1000 μm. The SFR for each galaxy is estimated using the $L_{\rm IR}$–SFR conversion in Kennicutt (1998) assuming a Salpeter (1955) IMF: SFR [$M_\odot$ yr^{-1}] $= 1.72 \times 10^{-10}$ $L_{\rm IR}$. This technique of FIR SED modelling is applied to the 5MUSES sample including 165 galaxies. In addition, we estimate monochromatic dust luminosities using the *Spitzer* MIPS (24 and 160 μm) and *Herschel* SPIRE photometric

Table 1. CO(1–0) line observations of the 5MUSES targets from our programs.

ID[a]	RA [hh:mm:ss]	Dec. [dd:mm:ss]	z_{co}	FWHM[e] [km s^{-1}]	$S_{CO}\Delta v$ [Jy km s^{-1}]	$\log(L'_{CO}$[d])	rms[f] [mK]
20	02:19:09.6	−05:25:12.9	0.098[b]	–	<0.16	<7.87	0.94
22	02:19:16.1	−05:57:27.0	0.103	311 ± 84	1.79 ± 0.47	8.95 ± 0.11	0.30
28	02:19:53.0	−05:18:24.2	0.073	261 ± 73	5.94 ± 1.40	9.16 ± 0.10	0.61
36	02:21:47.9	−04:46:13.5	0.025[b]	–	<0.65	<7.27	0.57
64	02:25:48.2	−05:00:51.5	0.150[c]	–	<0.31	<8.52	0.29
66	02:26:00.0	−05:01:45.3	0.205	274 ± 59	2.37 ± 0.45	9.69 ± 0.08	0.16
75	02:27:41.6	−04:56:50.6	0.055	173 ± 61	3.27 ± 0.85	8.66 ± 0.11	0.07
86	10:36:46.4	+58:43:30.6	0.140	307 ± 80	2.58 ± 0.71	9.38 ± 0.12	0.28
106	10:44:38.2	+56:22:10.8	0.024	375 ± 68	15.22 ± 2.38	8.64 ± 0.07	1.31
107	10:44:54.1	+57:44:25.8	0.118	345 ± 74	3.59 ± 0.79	9.37 ± 0.10	0.21
118	10:49:07.2	+56:57:15.4	0.071	–	<3.55	<8.93	0.80
123	10:50:06.0	+56:15:00.0	0.118	215 ± 56	2.65 ± 0.63	9.25 ± 0.10	0.21
146	10:59:03.5	+57:21:55.1	0.117[b]	–	<0.87	<8.76	0.51
152	11:01:33.8	+57:52:06.6	0.275	285 ± 89	3.71 ± 1.15	10.15 ± 0.13	0.24
185	16:08:58.4	+55:30:10.3	0.065	221 ± 38	3.40 ± 0.66	8.84 ± 0.08	0.37
187	16:09:07.6	+55:24:28.4	0.065	396 ± 300	5.28 ± 1.07	9.01 ± 0.09	0.39
188	16:09:08.3	+55:22:41.5	0.085	313 ± 73	5.28 ± 1.07	9.01 ± 0.09	0.54
191	16:09:31.6	+54:18:27.4	0.086	645 ± 165	7.58 ± 1.67	9.38 ± 0.10	0.36
192	16:09:37.5	+54:12:59.3	0.086	294 ± 136	3.28 ± 0.64	9.06 ± 0.08	0.13
196	16:12:23.4	+54:03:39.2	0.138	210 ± 65	1.93 ± 0.53	9.24 ± 0.12	0.18
197	16:12:33.4	+54:56:30.5	0.084	279 ± 38	7.76 ± 1.13	9.40 ± 0.06	0.88
198	16:12:41.1	+54:39:56.8	0.035[b]	–	<1.23	<7.84	0.61
200	16:12:50.9	+53:23:05.0	0.047	–	<5.50	<8.77	0.85
202	16:12:54.2	+54:55:25.4	0.065	–	<5.48	<9.03	0.99
294	17:12:32.4	+59:21:26.2	0.210	307 ± 55	2.00 ± 0.26	9.64 ± 0.06	0.03
297	17:13:16.6	+58:32:34.9	0.079	437 ± 101	3.62 ± 0.97	9.02 ± 0.12	0.33
302	17:14:46.4	+59:33:59.8	0.131	–	<3.49	<9.44	0.75
310	17:17:11.1	+60:27:10.0	0.110	350 ± 99	3.15 ± 0.79	9.26 ± 0.11	0.17
315	17:19:33.3	+59:27:42.7	0.139	423 ± 131	3.85 ± 1.05	9.55 ± 0.12	0.42
316	17:19:44.9	+59:57:07.1	0.069	–	<2.15	<9.03	1.36
317	17:20:43.3	+58:40:26.9	0.125	329 ± 152	2.81 ± 0.73	9.32 ± 0.11	0.11
319	17:21:59.3	+59:50:34.2	0.028	168 ± 46	7.67 ± 1.96	8.44 ± 0.11	0.51
328	17:25:46.8	+59:36:55.3	0.035	393 ± 137	13.89 ± 2.53	8.89 ± 0.08	0.24
329	17:25:51.3	+60:11:38.9	0.029	171 ± 35	9.10 ± 1.67	8.54 ± 0.08	0.04

Notes. [a]5MUSES ID name.
[b]The NASA/IPAC Extragalactic Data base (NED) is operated by the Jet Propulsion Laboratory, California Institute of Technology, under contract with the National Aeronautics and Space Administration. [c]For sources with CO(1–0) 3σ upper limits, the redshift is derived from the IRS spectra (b) or obtained from the NASA/IPAC Extragalactic Data base (c) as listed in Wu et al. (2010).
[d]L'_{CO} luminosities are in units of [K km s^{-1} pc^2].
[e]The CO line width is estimated by measuring the full width at half-maximum (FWHM) of the Gaussian profile.
[f] For galaxies with $>3\sigma$ CO detection and upper limits, we list the RMS of the CO line and the baseline, respectively.

Table 2. Data sample overview.

Sample	N	z	$\log(L_{IR}/L_{\odot})$	PAH feature	CO line	References [PAH, CO]
SINGS	36	0.001–0.007	7.31–10.60	6.2 μm	(3–2)	S07, W12
Local ULIRGs	9, (9)	0.018–0.191	11.99–12.42	6.2 μm, 7.7 μm	(1–0)	P13
5MUSES	22, (24)	0.025–0.277	9.23–11.81	6.2 μm, 7.7 μm	(1–0)	W10, this paper
5MUSES	14, (15)	0.053–0.360	10.35–12.10	6.2 μm, 7.7 μm	(1–0)	W10, K14
high-z SFGs	4, (3)	1.016–1.523	11.86–12.66	6.2 μm, 7.7 μm	(1–0), (2–1)	P13
SMGs	6, (8)	1.562–4.055	12.30–13.08	6.2 μm, 7.7 μm	(1–0), (2–1), (3–2), (4–3)	P13
High-z SBs	(6)	1.562–2.470	12.55–12.93	6.2 μm, 7.7 μm	(2–1), (3–2)	Sa07, Y07

Notes. The table includes all galaxies with at $3 \geq \sigma$ CO and PAH detections.
Column (1): Galaxy sample; column (2): Number of galaxies with PAH 6.2 μm (and 7.7 μm) detections; column (3): Redshift range; column (4): IR luminosity range; column (5): Detected PAH feature; column (6): Observed CO transition line; column (7): References: S07: Smith et al. (2007), W12: Wilson et al. (2012), P13: Pope et al. (2013) and references therein, W10: Wu et al. (2010), K14: Kirkpatrick et al. (2014), Sa07: Sajina et al. (2007), Y07: Yan et al. (2007).

bands (250, 350, and 500 μm). We derive PAH luminosities from the *Spitzer* IRS data using PAHFIT. For galaxies in the literature where the PAH luminosities have been estimated using the spline method, we derive the PAH luminosities using PAHFIT to ensure that the PAH 6.2 and 7.7 μm emissions have been estimated in a consistent way for both our targets and the literature compilation.

To summarize, the full sample with both detected CO, PAH 6.2 μm, and IR emission contains 36 5MUSES galaxies (including

Table 3. General properties of the 5MUSES sample.

ID[a]	RA [hh:mm:ss]	Dec. [dd:mm:ss]	z	$\log(L_{6.2}/L_\odot)$[b]	$EW_{6.2}$ [μm]	$\log(L_{7.7}/L_\odot)$[b]	$\log(M_*/M_\odot)$[c]	$\log(L_{IR}/L_\odot)$	$\log(M_{dust}/M_\odot)$	$\log(M_{H_2}/M_\odot)$
2	02:15:03.5	−04:24:21.7	0.137	8.58 ± 0.19	0.78 ± 0.01	9.19 ± 0.14	10.51	10.86 ± 0.04	8.01 ± 0.28	10.01
4	02:15:57.1	−03:37:29.1	0.032	7.59 ± 0.08	0.50 ± 0.05	8.09 ± 0.09	9.97	9.83 ± 0.02	7.18 ± 0.29	9.18
5	02:16:38.2	−04:22:50.9	0.304	9.06 ± 0.24	<0.09	9.48 ± 0.11	10.80	11.54 ± 0.02[d]	–	–
6	02:16:40.7	−04:44:05.1	0.870	9.13 ± 1.62	<0.05	–	11.82	12.70 ± 0.01[d]	–	–
8	02:16:49.7	−04:25:54.8	0.143	9.01 ± 0.09	1.11 ± 0.06	9.48 ± 0.08	10.06	10.99 ± 0.01	7.29 ± 0.42	9.29
–	–	–	–	–	–	–	–	–	–	–

Notes. Column (1): Source name; column (2): Right ascension in units of hours, minutes, and seconds; column (3): Declination in units of degrees, arcminutes, and arcseconds; column (4): Redshift; column (5): PAH 6.2 μm luminosity; column (6): Equivalent width of the PAH 6.2 μm feature; column (7): PAH 7.7 μm luminosity; column (8): Stellar mass; column (9): Infrared luminosity (integrated from 8 to 1000 μm); column (10): Dust mass; column (13): Molecular gas mass derived using the M_{dust}–δ_{GDR} method.
[a]5MUSES ID name.
[b]PAH luminosity from Magdis et al. (2013).
[c]Stellar masses from Shi et al. (2011).
[d]L_{IR} from Shi et al. (2011).

Table 4. Galaxies from the literature with PAH, IR, and/or CO emission.

Name	RA [hh:mm:ss]	Dec. [dd:mm:ss]	Sample	z	$\log(L_{6.2}/L_\odot)$	$EW_{6.2}$ [μm]	$\log(L_{7.7}/L_\odot)$	$\log(L_{IR}/L_\odot)$	Line	$\log(L'_{CO}/L_\odot)$
NGC 3049	09:54:49.59	+09:16:18.1	SINGS	0.006	7.81 ± 0.02[a]	–	–	9.65 ± 0.02[a]	CO(3–2)	7.68 ± 0.21[b]
IRAS 10565 + 2448	10:59:18.12	+24:32:34.5	local ULIRGs	0.043	9.57 ± 0.01	–	–	12.04 ± 0.02[c]	CO(1–0)	9.72 ± 0.03[c]
GN26	12:36:34.51	+62:12:40.9	SMGs	1.223	10.48 ± 0.02	0.38 ± 0.04	11.01 ± 0.10	12.66 ± 0.17[c]	CO(2–1)	10.92 ± 0.12[c]
GN70.211	12:37:10.60	+62:22:34.5	High-z SFGs	1.523	10.39 ± 0.10	–	10.84 ± 0.12	11.94 ± 0.17[c]	CO(1–0)	10.20 ± 0.12[c]
MIPS506	17:11:38.59	+58:38:38.6	High-z SBs	2.470	–	0.30 ± 0.14[d]	11.11 ± 0.13	12.93 ± 0.09[e]	CO(3–2)	10.52 ± 0.09[e]
–	–	–	–	–	–	–	–	–	–	

Notes. Column (1): Source name; column (2): Right ascension in units of hours, minutes, and seconds; column (3): Declination in units of degrees, arcminutes, and arcseconds; column (4): Galaxy sample or selection; column (5): Redshift; column (6): PAH 6.2 μm luminosity; column (7): Equivalent width of the PAH 6.2 μm feature; column (8): Infrared luminosity (integrated from 8−1000 μm); column (9): Observed CO line; column (10): CO(1–0) luminosity.
[a]From Smith et al. (2007). IR luminosities are aperture corrected. [b]From Wilson et al. (2012). Converted to CO(1-0) luminosities using $r_{32/10} = 0.18 \pm 0.02$.
[c]From Pope et al. (2013). For the CO luminosities, we corrected higher J transitions using the conversion scheme listed in Bothwell et al. (2013): $r_{21/10} = 0.84 \pm 0.13$, $r_{32/10} = 0.52 \pm 0.09$, $r_{43/10} = 0.41 \pm 0.07$.
[d]From Sajina et al. (2007).
[e]From Yan et al. (2010).

5 AGNs and composite sources), 36 SINGS galaxies, nine local ULIRGs, four high-z SFGs, and six SMGs (See Table 2).

3 RESULTS

Previous works have studied scaling relations between the L_{IR}, L_{PAH}, and L'_{CO} of various galaxy populations across a wide range of redshifts (e.g. Calzetti et al. 2005; Smith et al. 2007; Bendo et al. 2008; Pope et al. 2013; Rujopakarn et al. 2013; Kirkpatrick et al. 2014). In this section, we will revisit these relations for our sample, attempting to identify outliers and investigate them not only as a function of lookback time but also as a function of physical conditions (AGN, SBs, normal galaxies, etc).

3.1 The relation between IR and PAH luminosity

As discussed in the Introduction, L_{PAH}/L_{IR} variations may not only be driven by the presence of an AGN and the geometry of the star formation but also by the metallicity and the hardness of the radiation field. To investigate the L_{PAH}/L_{IR} variations in different galaxy populations across a wide range of redshifts, we consider the $L_{6.2}$, $L_{7.7}$, and L_{IR} measurements for the 5MUSES sample as well as for other galaxies in the literature for which such measurements are available, including local ULIRGs (Armus et al. 2007; Desai et al. 2007), high-z ($1 < z < 4$) SMGs, BzKs and 70 μm selected galaxies (Pope et al. 2008; Pope et al. 2013, and references therein), and 24 μm selected SBs at $z \sim 2$ (Yan et al. 2010). Due to possible biases introduced from the aperture correction applied to the SINGS galaxies (Kennicutt et al. 2003), we omit them from the best-fitting regression models.

In Fig. 3, we plot the PAH 6.2 μm and 7.7 μm luminosities as a function L_{IR} for our full sample of galaxies and model the data in the logarithmic space using the Bayesian linear regression analysis as described in Kelly (2007). This method accounts for measurement errors of both the dependent and independent variables and it returns posterior distributions of the best-fitting parameters, including the intrinsic scatter. All the best-fitting parameters of the regression model: $\log y = \alpha \times \log x + \beta$ are listed in Table 5. Focusing only on local/intermediate redshift star-formation dominated sources and high-z SFGs that are part of the MS of star formation, we find a tight, linear correlation, with a slope of $\alpha = 0.98 \pm 0.03$ and intrinsic scatter of $\sigma = 0.13$ dex for the $L_{6.2}$–L_{IR} relation, while $\alpha = 1.00 \pm 0.03$ and $\sigma = 0.13$ dex for $L_{7.7}$–L_{IR}, in agreement with the best-fitting relations reported in Pope et al. (2008) and similar studies (e.g. Sajina et al. 2008; Rujopakarn et al. 2013; Shipley et al. 2016). The dispersion of the L_{PAH}/L_{IR} ratios as a function of L_{IR} and galaxy type is shown in the top panels of Fig. 3. From these relations, local ULIRGs (and high-z SBs with available $L_{7.7}$ estimates) exhibit systematically lower PAH/IR luminosity ratios. We quantify these galaxies as outliers lying 3.2σ from the best-fitting relations (2.5σ for $L_{7.7}$–L_{IR}). Fitting the full sample (excluding upper limits) yields a shallower slope but also an increased intrinsic scatter of $\sigma = 0.21$ dex and $\sigma = 0.20$ dex for the $L_{6.2}$–L_{IR} and $L_{7.7}$–L_{IR} relations, respectively. We note though, that a considerable fraction of local ULIRGs and high-z SBs are still outliers, even when attempting to fit the whole sample, in agreement with Shipley

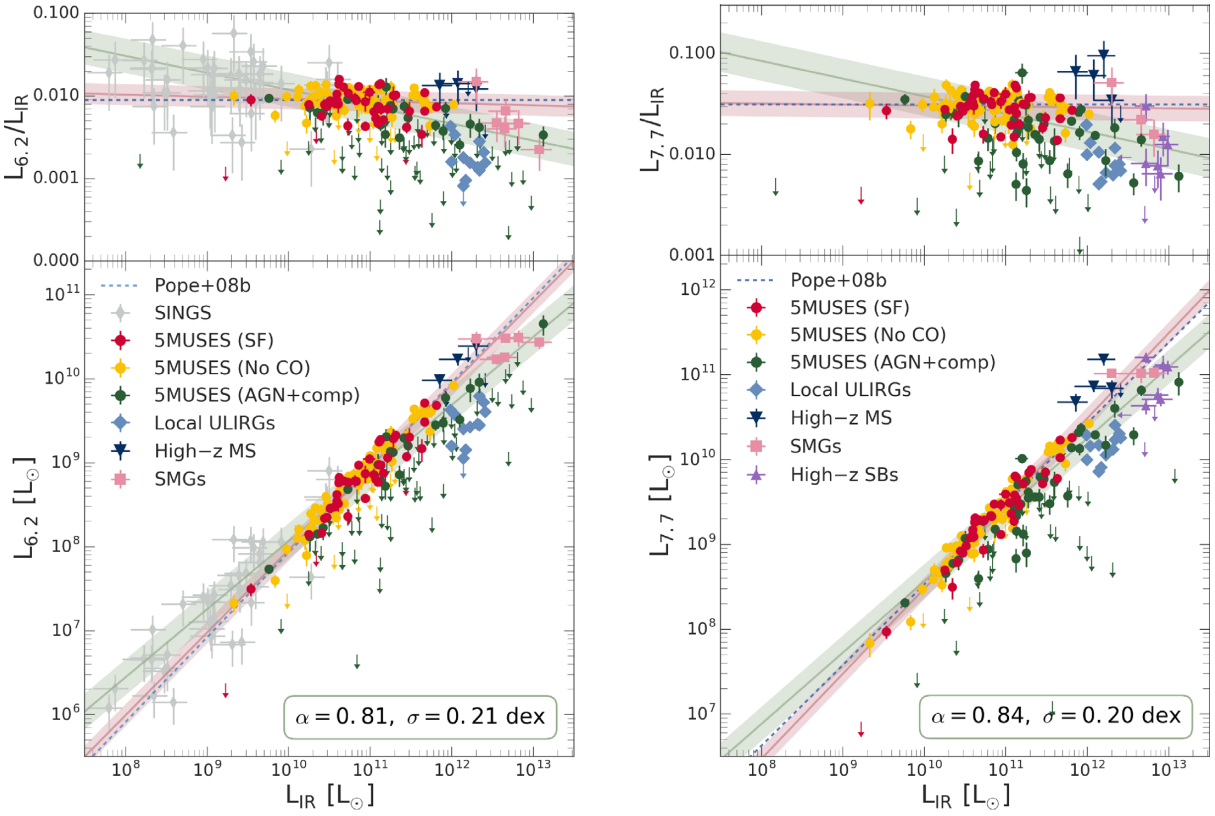

Figure 3. Correlation between the total infrared luminosity (L_{IR}) versus PAH 6.2 μm luminosity ($L_{6.2}$) (*left*) and PAH 7.7 μm luminosity ($L_{7.7}$) (*right*). For the 5MUSES sample, we include CO-detected SFGs (red), AGNs and composite sources (green), and the remaining sample of SFGs (yellow). $L_{6.2}$ and $L_{7.7}$ upper limits are shown as arrows. We also include SINGS galaxies (grey, only for $L_{6.2}$), local ULIRGs (light blue), high-z SFGs (dark blue), SMGs (pink), and high-z SBs (purple, only for $L_{7.7}$). The green and pink lines depict the L_{PAH}–L_{IR} linear regression models of the SFGs (5MUSES and high-z SFGs) and the full sample, respectively, excluding the SINGS sources as described in Section 2.2.2. The same method is applied to the L_{PAH}/L_{IR} versus L_{IR} relations presented in the upper panels. The shaded regions present the intrinsic scatter of the best fits. The blue dashed lines show the best-fitting relations from Pope et al. (2008) of local SBs and SMGs. For the upper panels, the dashed lines are the median value of the L_{PAH}/L_{IR} assuming L_{PAH}–L_{IR} slopes of unity.

et al. (2016). It is thus evident that a universal L_{IR}–$L_{6.2}$ relation, accommodating the various physical conditions of different galaxy populations, cannot be established.

3.2 The CO–IR luminosity relation

The use of L_{IR} as an SFR tracer and the fact that CO emission is directly associated with the molecular gas reservoir of a galaxy has motivated several studies to investigate the L'_{CO}–L_{IR} relation as a proxy for the star formation law that links the SFR to the molecular gas of galaxies (KS law). The existence of a universal L'_{CO}–L_{IR} (and thus of a universal M_{gas}–SFR) relation has been challenged by recent observations of different galaxy populations at various redshifts (e.g. Bouché et al. 2007; Daddi et al. 2010b; Genzel et al. 2010; Krumholz, Dekel & McKee 2012; Silverman et al. 2015). Although the debate is still open, there are claims that MS galaxies at all redshifts tend to follow a unique L'_{CO}–L_{IR} relation from which local ULIRGs and high-z SBs are outliers exhibiting lower L'_{CO}/L_{IR} ratios, indicative of higher SFEs (e.g. Daddi et al. 2010b; Genzel et al. 2010, Magdis et al. 2017). Addressing the question of this possible bimodality is beyond the scope of our work. Instead, we wish to investigate how the galaxies at different redshifts and with different physical conditions populate the L'_{CO}–L_{IR} parameter space and explore how the global L'_{CO}–L_{IR} relation behaves with respect to the observed trends between L_{PAH}–L_{IR} and L_{PAH}–L'_{CO}.

In Fig. 4, we present the L_{IR}–L'_{CO} relation for the 5MUSES sample along with the literature compilation included in Fig. 3 (See Table 2). We also consider the L_{IR}–L'_{CO} relation of Sargent et al. (2014) calibrated on MS galaxies with $M_* \geq 10^{10}$ $M_\odot$ at $0 < z < 3.2$ with a slope of 0.81 and a dispersion of 0.21 dex. The vast majority of SFGs, including our 5MUSES sample and the high-z SFGs appear to follow the Sargent relation. On the other hand, local ULIRGs and high-z SBs are outliers, a situation that resembles the $L_{6.2}$–L_{IR} and $L_{7.7}$–L_{IR} relations (Fig. 3). In other words, sources exhibiting lower L'_{CO}/L_{IR} ratios with respect to the general population of normal galaxies tend to also exhibit lower L_{PAH}/L_{IR} ratios. In the next subsection, we bring these two together by exploring the relations between PAH and CO luminosities.

3.3 The relations between CO and PAH emission

In Fig. 5, we plot the $L_{6.2}$ versus L'_{CO} (*left*) and $L_{7.7}$ versus L'_{CO} (*right*) luminosity relations for the 5MUSES sample as well as for the whole data set confirming the observed correlation between the PAH 6.2 μm and CO emission (Pope et al. 2013). The various populations appear to follow a unique relation, with a slope of unity

Table 5. Linear scaling relations between the emission from PAHs, IR, and CO, and various galaxy properties.

log x	log y	α	β	σ	Sample
$L_{\rm IR}$ [$L_\odot$]	$L_{6.2}$ [$L_\odot$]	0.98 ± 0.03	-1.89 ± 0.30	0.13	SFGs
$L_{\rm IR}$ [$L_\odot$]	$L_{6.2}$ [$L_\odot$]	0.81 ± 0.03	-0.04 ± 0.29	0.21	All
$L_{\rm IR}$ [$L_\odot$]	$L_{7.7}$ [$L_\odot$]	1.00 ± 0.03	-1.53 ± 0.28	0.13	SFGs
$L_{\rm IR}$ [$L_\odot$]	$L_{7.7}$ [$L_\odot$]	0.84 ± 0.02	-0.15 ± 0.26	0.20	All
$L'_{\rm CO}$ [K km s^{-1} pc^2]	$L_{6.2}$ [$L_\odot$]	1.02 ± 0.06	-0.65 ± 0.31	0.24	SFGs
$L'_{\rm CO}$ [K km s^{-1} pc^2]	$L_{6.2}$ [$L_\odot$]	1.03 ± 0.06	-0.73 ± 0.38	0.26	All
$L'_{\rm CO}$ [K km s^{-1} pc^2]	$L_{6.2}$ [$L_\odot$]	0.99 ± 0.07	-0.37 ± 0.70	0.24	With CO(1–0)
$L'_{\rm CO}$ [K km s^{-1} pc^2]	$L_{7.7}$ [$L_\odot$]	1.03 ± 0.08	-0.13 ± 0.19	0.21	SFGs
$L'_{\rm CO}$ [K km s^{-1} pc^2]	$L_{7.7}$ [$L_\odot$]	1.04 ± 0.08	-0.21 ± 0.20	0.23	All
L_{24} [$L_\odot$]	$L_{6.2}$ [$L_\odot$]	0.99 ± 0.05	1.51 ± 0.37	0.20	5MUSES SFGs
L_{24} [$L_\odot$]	$L_{6.2}$ [$L_\odot$]	0.90 ± 0.05	2.14 ± 0.35	0.21	5MUSES
L_{160} [$L_\odot$]	$L_{6.2}$ [$L_\odot$]	1.02 ± 0.04	-0.11 ± 0.37	0.11	5MUSES
L_{250} [$L_\odot$]	$L_{6.2}$ [$L_\odot$]	0.87 ± 0.04	1.48 ± 0.31	0.17	5MUSES
L_{350} [$L_\odot$]	$L_{6.2}$ [$L_\odot$]	0.87 ± 0.05	1.83 ± 0.38	0.19	5MUSES
L_{500} [$L_\odot$]	$L_{6.2}$ [$L_\odot$]	0.83 ± 0.06	2.34 ± 0.42	0.17	5MUSES
$L_{6.2}$ [$L_\odot$]	$L_{7.7}$ [$L_\odot$]	1.00 ± 0.02	0.62 ± 0.13	0.01	5MUSES
L_{24} [$L_\odot$]	$L_{7.7}$ [$L_\odot$]	0.97 ± 0.05	2.15 ± 0.37	0.21	5MUSES SFGs
L_{24} [$L_\odot$]	$L_{7.7}$ [$L_\odot$]	0.79 ± 0.05	3.46 ± 0.40	0.28	5MUSES
L_{160} [$L_\odot$]	$L_{7.7}$ [$L_\odot$]	1.04 ± 0.04	0.23 ± 0.37	0.12	5MUSES
L_{250} [$L_\odot$]	$L_{7.7}$ [$L_\odot$]	0.87 ± 0.04	2.03 ± 0.3	0.19	5MUSES
L_{350} [$L_\odot$]	$L_{7.7}$ [$L_\odot$]	0.85 ± 0.05	2.45 ± 0.40	0.22	5MUSES
L_{500} [$L_\odot$]	$L_{7.7}$ [$L_\odot$]	0.82 ± 0.06	3.00 ± 0.48	0.22	5MUSES
$L_{6.2}$ [$L_\odot$]	$L_{7.7}$ [$L_\odot$]	1.00 ± 0.02	0.62 ± 0.13	0.01	5MUSES
$L_{6.2}$ [$L_\odot$]	$L_{7.7}$ [$L_\odot$]	1.02 ± 0.02	0.36 ± 0.19	0.06	All
$L_{6.2}$ [$L_\odot$]	$M_{\rm H_2}$[a] [$M_\odot$]	1.00 (fixed)	1.10 ± 0.01	0.28	5MUSES MS SFGs[b]
$L_{7.7}$ [$L_\odot$]	$M_{\rm H_2}$[a] [$M_\odot$]	1.00 (fixed)	0.55 ± 0.02	0.28	5MUSES MS SFGs[b]

Notes. The linear fits are obtained in the logarithmic space : $\log y = \alpha \times \log x + \beta$. The best-fitting parameters and the intrinsic scatter are estimated from the Bayesian linear regression method described in Kelly (2007).
[a]Dust-derived molecular gas masses assuming solar metallicity.
[b]With $\log(M_*/M_\odot) > 10$.

within the uncertainties ($L_{6.2}$–$L'_{\rm CO}$: $\alpha = 1.03 \pm 0.06$ and $L_{7.7}$–$L'_{\rm CO}$: $\alpha = 1.04 \pm 0.08$), in agreement with the slightly sub-linear slope ($\alpha = 0.9 \pm 0.01$) reported in Pope et al. (2013). The $L_{6.2}$–$L'_{\rm CO}$ and $L_{7.7}$–$L'_{\rm CO}$ relations have an intrinsic scatter of $\sigma = 0.26$ dex and $\sigma = 0.23$ dex, respectively, without any specific SFG population standing out as prominent outliers. The shaded regions in the upper panels of Fig. 5 depict the intrinsic scatter of $L_{6.2}$–$L'_{\rm CO}$ and $L_{7.7}$–$L'_{\rm CO}$ correlations assuming a slope of unity. In order to ensure that the linear slopes of the $L_{\rm PAH}$–$L'_{\rm CO}$ correlations are not affected by corrections applied to galaxies with higher J CO observations, we fit only those galaxies with CO(1–0) emission yielding a slope of $\alpha = 0.99 \pm 0.07$ consistent with the best fit of the full sample. The global PAH–CO luminosity relation for $L_{6.2}$ is parametrized as:

$$L_{6.2}\ [{\rm L}_\odot] = (0.39 \pm 0.18) \times {\rm L}'_{\rm CO}\ [{\rm K\ km\ s^{-1}\ pc^2}]. \quad (2)$$

The universal $L_{6.2}$–$L'_{\rm CO}$ and $L_{7.7}$–$L'_{\rm CO}$ relations as indicated by our data suggest a link between the PAH and CO emission that appears unaffected by the physical conditions of the galaxies. Since the CO emission is a tracer of the gas mass and thus of the cold dust emission, a natural consequence of the $L_{\rm PAH}$–$L'_{\rm CO}$ is a link between the PAH and the cold dust emission of a galaxy. This is explored in detail in the following section.

3.4 The relation between PAH and dust emission

In the previous section, we showed that the emission from PAHs on global scales correlate with CO(1–0) luminosity over a wide range of redshifts and various galaxy types. This result suggests a link between the PAH emission and the $M_{\rm gas}$ of a galaxy. Since $M_{\rm gas}$ is a derived physical parameter rather than a direct observable, before exploring a possible $L_{\rm PAH}$–$M_{\rm gas}$ relation, it is informative to investigate the scaling relations and the scatter between $L_{\rm PAH}$ and the warm and the cold dust emission through MIR and FIR photometric bands. The motivation behind this exercise is that $M_{\rm gas}$ is known to be directly associated with the cold dust emission of galaxies (Leroy et al. 2011; Eales et al. 2012; Magdis et al. 2012; Magdis et al. 2013; Scoville et al. 2017), whereas the warm dust emission is linked to star formation. For the sake of brevity and clarity, we only present the results for the PAH 6.2 μm feature which is least affected by silicate absorption and extinction (Peeters, Spoon & Tielens 2004). However, the same applies to the PAH 7.7 μm feature due to the linear correlation between these two in logarithmic scales ($L_{6.2}$–$L_{7.7}$: $\alpha = 1.02 \pm 0.02$, see Table 5).

Using *Spitzer* and *Herschel* photometric observations of the 5MUSES sample, we derive monochromatic luminosities at 24, 160, 250, 350, and 500 μm (see Section 2.3) and plot them against $L_{6.2}$ in Figs 6 and 7, including galaxies with secure dust luminosities ($>3\sigma$). To minimize the effects of K-correction, we restrict our sample to a redshift range of $0.1 < z < 0.3$ ($\langle z \rangle = 0.12 \pm 0.05$). While $L_{6.2}$ is found to correlate with both the warm dust emission as traced by L_{24} as well as with the colder dust emission (at L_{160}, L_{250}, L_{350}, and L_{500}), we obtain a lower scatter for the latter, even when AGNs are excluded from the fit. We note that quite naturally galaxies with the presence of an AGN appear as prominent outliers

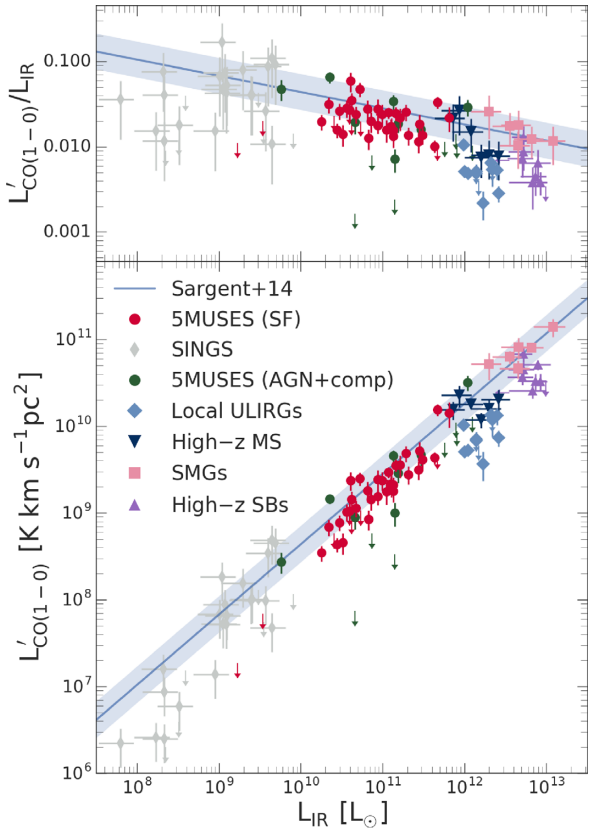

Figure 4. Correlation between CO(1–0) line luminosity (L'_{CO}) and L_{IR}. Colour coding and symbols follow Fig. 3. Higher-J CO transitions from the literature are corrected to CO(1–0) using Wilson et al. (2012) for the SINGS galaxies and Bothwell et al. (2013) are adopted for the remaining sample. The blue lines show the L'_{CO}–L_{IR} relation from Sargent et al. (2014). The top panel shows the L'_{CO}/L_{IR} ratio in units of [(K km s^{-1} pc^2)/L$_\odot$] as a function of L_{IR} along with the Sargent et al. (2014) relation. The blue shaded regions depict the observed dispersion of 0.21 dex.

only in the $L_{6.2}$−L_{24} relation due to the intrinsic AGN dust emission that peaks between rest frame 15 and 60 μm (Mullaney et al. 2011), boosting the L_{24} (for fixed L_{IR}) with respect to star-formation dominated galaxies.

The correlation between the cold dust and PAH emission has been supported by various spatially resolved observations of local galaxies. For example, using *Spitzer* observations of local normal galaxies, Bendo et al. (2008) find the PAH emission to be well correlated with the 160 μm emission on spatial scales of ∼2 kpc, and a significant scatter in the relation between PAH and 24 μm emission, concluding that the PAHs are associated with the diffuse, cold dust. Similar results, based on SMC observations, were reached by Sandstrom et al. (2010, 2012), who also reported a strong correlation between the PAH and CO(1–0) emission. Furthermore, Haas et al. (2002), find a good spatial coincidence between the 850 μm continuum emission and the strength of the PAH 7.7 μm line, suggesting again that the PAH carriers are preferentially related to the regions dominated by cold dust and molecular clouds, where they are excited mainly by the interstellar radiation field.

These findings are also in agreement with recent modelling studies of the various dust components within H II regions and their surrounding envelopes (Pavlyuchenkov et al. submitted; see also Akimkin et al. 2015, 2017). They argue for a lower correlation between PAHs and graphite grains, responsible for the majority of the dust emission at 24 μm, due to possible destruction of PAHs within the H II regions. By modelling the intensity distributions of the different dust components, they find similar intensity distributions between PAHs and silicates that are the dominant dust component at ∼100–500 μm. This could indicate that PAHs located in the molecular clouds are excited by escaping UV photons from the H II regions (Pavlyuchenkov et al. submitted).

Put together, our analysis suggests that on global integrated scales PAH emission is linked to the cold dust and the CO emission in our sample, both of which are tracers of the molecular gas.

3.5 The $L_{6.2}$–M_{H_2} relation in MS galaxies

The total molecular gas mass can be estimated from the observed CO luminosity, assuming a CO–H_2 conversion factor, α_{CO}: $M_{H_2}[M_\odot] = \alpha_{CO} \times L'_{CO}$. Corollary, the linear relation between $L_{6.2}$ and L'_{CO} ratio presented in the previous section, can be used to convert $L_{6.2}$ to molecular gas masses. Using the median $L_{6.2}/L'_{CO}$ ratio of (0.37 ± 0.18) $L_\odot/(K\,km\,s^{-1}\,pc^2)$ as indicated by our data, we define:

$$M_{H_2}\ [M_\odot] = \alpha_{CO} \times (2.7 \pm 1.3) \times L_{6.2}. \quad (3)$$

However, both observational and theoretical studies suggest that α_{CO} varies with specific properties of the ISM, including metallicity and galaxy morphology (e.g. Leroy et al. 2011; Narayanan et al. 2012; Papadopoulos et al. 2012; Sandstrom et al. 2013), ranging between $\langle\alpha_{CO}\rangle \approx 4.5\ M_\odot/(K\,km\,s^{-1}\,pc^2)$ for normal MS galaxies and $\langle\alpha_{CO}\rangle \approx 0.8\ M_\odot/(K\,km\,s^{-1}\,pc^2)$ for local ULIRGs and high-z SBs (e.g. Solomon et al. 1987; Tacconi et al. 2006; Tacconi et al. 2008; Daddi et al. 2010b; Leroy et al. 2011; Magdis et al. 2011; Magdis et al. 2012; Casey, Narayanan & Cooray 2014).

To avoid the dependency on α_{CO}, we derive molecular gas mass estimates using the FIR dust continuum observations. This method relies on the fact that M_{gas} can be derived from the dust mass by exploiting the well-calibrated gas-to-dust mass ratio ($\delta_{GDR}(Z)$) (e.g. Leroy et al. 2011; Magdis et al. 2012; Berta et al. 2016; Tacconi et al. 2018):

$$\delta_{GDR} \times M_{dust} \equiv M_{gas} = M_{H_I} + M_{H_2}, \quad (4)$$

where M_{H_I} is the atomic gas mass. Although the atomic-to-molecular gas ratio is not known at high redshift, current models suggest M_{H_2} dominates over M_{H_I} at high-z and high stellar surface densities (e.g. Blitz & Rosolowsky 2006; Obreschkow et al. 2009) and thus $M_{gas} \approx M_{H_2}$. Since the method is metallicity dependent, and in the absence of direct metallicity estimates, we choose to restrict our sample to massive galaxies with $\log(M_*/M_\odot) > 10$ that are known to follow the mass–metallicity relation as well as the FMR relation (e.g. Mannucci et al. 2010) at least out to $z \sim 2$. Moreover, whether SB systems, like local ULIRGs, follow the FMR relation or whether they are more metal-rich with respect to normal galaxies at fixed stellar mass is still an open debate (e.g. Magdis et al. 2011; Magdis et al. 2012; Silverman et al. 2015; Pereira-Santaella et al. 2017; Rigopoulou et al. 2018). To avoid the uncertainties and systematics introduced by the metallicity of SB galaxies, we choose to omit them from our analysis in this section. Instead, we focus on massive MS galaxies from the 5MUSES sample with sufficient FIR coverage (out to $\lambda_{rest} > 250$ μm to ensure robust M_{dust} estimates).

Molecular gas masses are then inferred using the δ_{GDR}–Z metallicity relation: $\log \delta_{GDR} = (10.54 \pm 1.0)$–$(0.99 \pm 0.12) \times (12 + \log(O/H))$ from Magdis et al. (2012). The resulting M_{H_2} estimates versus $L_{6.2}$ are presented in Fig. 8, yielding:

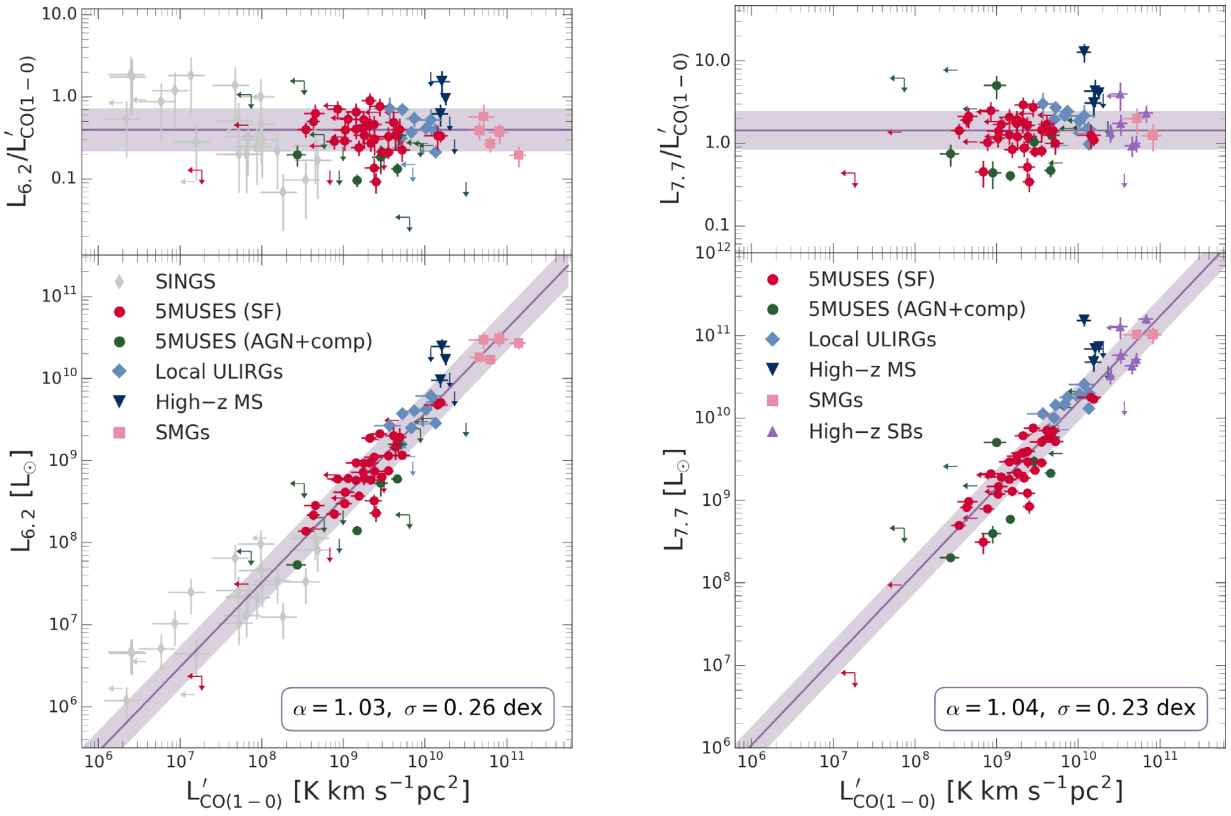

Figure 5. Correlation between $L_{6.2}$ versus L'_{CO}(*left*) and $L_{7.7}$ versus L'_{CO} (*right*). Colour coding and symbols follow Fig. 3. The top panels show the PAH and CO luminosity ratios in units of [$L_\odot$/(K km s^{-1} pc^2)] and as a function of L'_{CO}. SINGS galaxies (grey) are excluded from the fitting procedure due to possible systematics introduced from the applied aperture correction (See Section 2.2.2). The purple lines and shaded regions depict the best-fitting linear regression and its intrinsic scatter for all the galaxies. For the upper panels, we show the observed dispersion assuming a L_{PAH}–L'_{CO} slope of unity. The fit parameters of the CO–PAH luminosity relations are listed in Table 5.

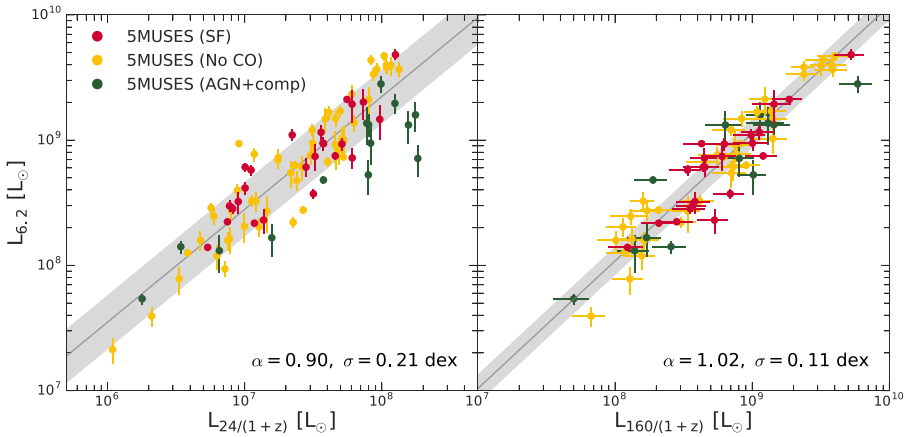

Figure 6. Correlation between $L_{6.2}$ and the 24 μm (*left*) and 160 μm luminosity (*right*) for the 5MUSES sample. Colour coding follow Fig. 3. The dark grey line depicts the best linear regression fit to the 5MUSES sample and the 1σ dispersion of the correlation presented as the shaded region. Note the reduced intrinsic scatter of the $L_{6.2}$−L_{160} relation as opposed to $L_{6.2}$−L_{24} and the fact that AGN/composite sources are clear outliers in the $L_{6.2}$−L_{24} relation. The fit parameters are listed in Table 5.

$$\log\left(\frac{M_{H_2}}{M_\odot}\right) = \log\left(\frac{L_{6.2}}{L_\odot}\right) + (1.10 \pm 0.02) \quad (5)$$

with an intrinsic scatter of $\sigma = 0.28$ dex. As a sanity check, we also overplot the M_{H_2}–$L_{6.2}$ relation using equation 3, adopting $\alpha_{CO} = 4.5$ $M_\odot$/(K km s^{-1} pc^2), a typical value for normal SFGs. Indeed, we see that this relation is in excellent agreement with our data, reassuring that both the dust-based M_{H_2} estimates and the L'_{CO}-based M_{H_2} estimates with $\alpha_{CO} = 4.5$ $M_\odot$/(K km s^{-1} pc^2) are consistent. Finally, we overplot equation 3 assuming $\alpha_{CO} = 0.8$ $M_\odot$/(K km s^{-1} pc^2) to indicate the expected location of SBs in Fig. 8. An attempt to explain the physical origin of the derived $L_{6.2}$–M_{H_2} relation and a discussion of its importance and limitations are presented in the following section.

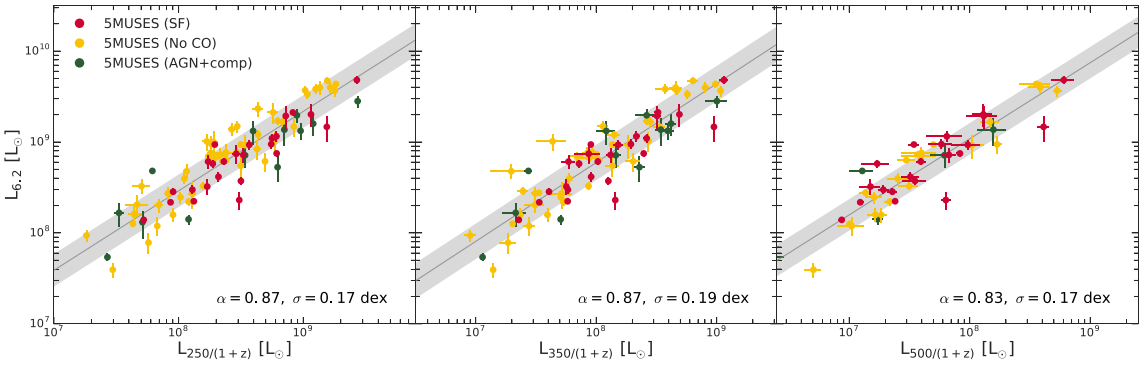

Figure 7. Correlation between $L_{6.2}$ and the 250 μm (*left*), 350 μm (*middle*), and 500 μm luminosity (*right*) for the 5MUSES sample. The fit parameters are listed in Table 5.

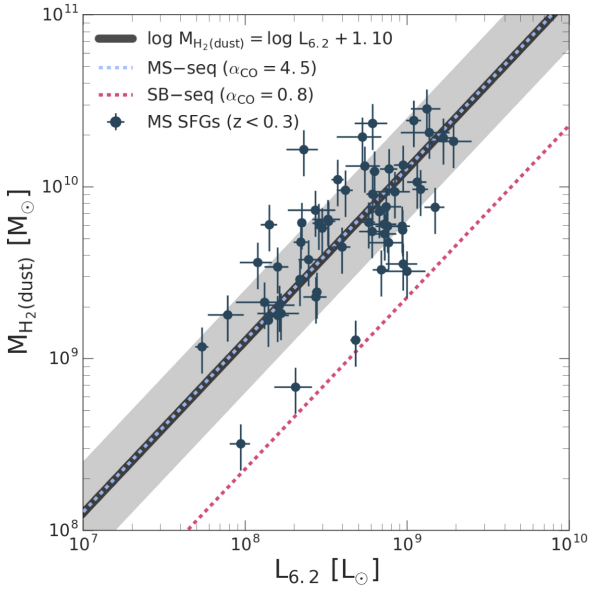

Figure 8. Correlation between $L_{6.2}$ and dust-derived molecular gas mass (M_{H_2}) for normal galaxies assuming solar metallicity. The sample includes 5MUSES MS galaxies at $z < 0.3$ with $\log(M_*/M_\odot) > 10$. The black line corresponds to the best fit with a fixed slope of 1 with an intrinsic scatter of 0.30 dex (grey shaded region). The light blue and red dashed lines are the M_{H_2}–L'_{CO} relation for MS and SB galaxies adopting $\alpha_{CO} = 4.5$ $M_\odot/(K\,km\,s^{-1}\,pc^2)$ and $\alpha_{CO} = 0.8$ $M_\odot/(K\,km\,s^{-1}\,pc^2)$, respectively.

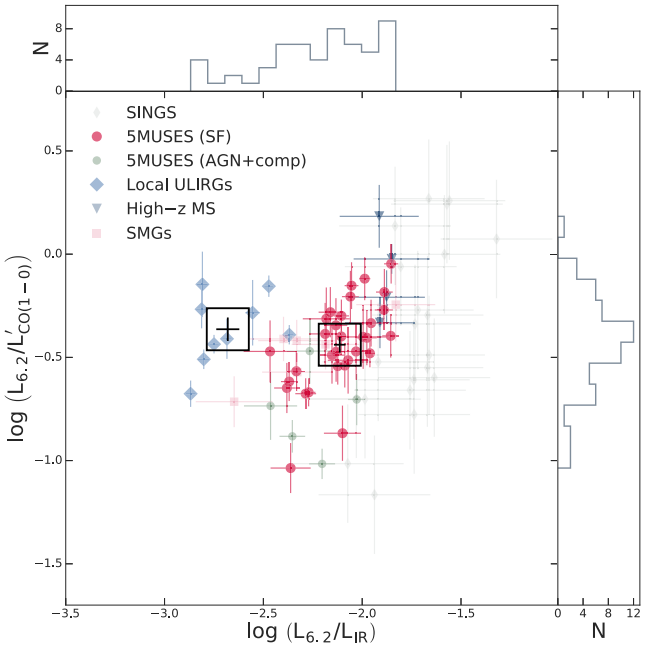

Figure 9. $\log(L_{6.2}/L'_{CO})$ versus $\log(L_{6.2}/L_{IR})$ for the full sample with both PAH and CO emission. Colour coding and symbols follow Fig. 3. The black open squares correspond to the median values for the 5MUSES SFGs and the local ULIRGs. The top and right panels show the distribution of $L_{6.2}/L_{IR}$ and $L_{6.2}/L'_{CO}$, respectively.

4 DISCUSSION

In the previous sections, we have explored the global scaling laws between $L_{6.2}$, L'_{CO}, and L_{IR} for a large compilation of different galaxy populations at various redshifts. We have seen that variations in the $L_{6.2}/L_{IR}$ and L'_{CO}/L_{IR} ratios among different galaxy populations are not permeated in their $L_{6.2}/L'_{CO}$ ratios that instead appear to be rather constant through a universal $L_{6.2}$–L'_{CO} relation with a slope of unity.

This is further demonstrated in Fig. 9. While the distribution of the $\log(L_{6.2}/L'_{CO})$ ratios is symmetric around the central value, we find a negatively skewed distribution of the $\log(L_{6.2}/L_{IR})$ ratios. This skewness is driven by systematically lower $\log(L_{6.2}/L_{IR})$ ratios of local ULIRGs. In fact, we find a 8.70σ significant difference between the mean values of $\log(L_{6.2}/L_{IR})$ for the local ULIRGs (-2.68 ± 0.06) and the 5MUSES SFGs (-2.11 ± 0.03). On the other hand, we do not find any significant systematic variations in the $\log(L_{6.2}/L'_{CO})$ ratios (ULIRGs: 0.36 ± 0.06, 5MUSES SFGs: 0.44 ± 0.04). This suggests that $L_{6.2}$ is, in fact, a better tracer of CO (and thus of M_{H_2}) than the total IR emission.

While the emerging PAH–CO luminosity relation has also been reported in spatially resolved observation of local galaxies, its physical origin (if any) is still debated. Bendo et al. (2010) suggest that the correlation between PAH and CO emission observed in NGC 2403 on large scales can be explained if they share similar excitation mechanisms, or if the molecular cloud formation is triggered in regions with stellar potential wells as described in Leroy et al. (2008). For the latter, CO emission could then arise from newly formed molecular clouds, while starlight in the potential wells would heat surrounding regions enhancing the PAH emission. This scenario would also explain the variations between PAH and CO emission on sub-kpc scales and the similar radial profiles on larger spatial scales (Regan et al. 2006). Finally, recent studies have suggested that

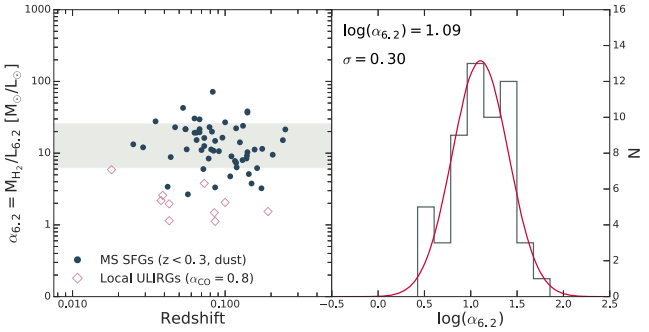

Figure 10. *Left*: Correlation between the $\alpha_{6.2}$ conversion factor versus redshift. The sample includes dust-derived $M_{\rm gas}$ estimates of 5MUSES MS galaxies at $z < 0.3$ (dark blue). The grey region depicts the average $\alpha_{6.2}$ value of the sample and the 1σ dispersion. We overplot local ULIRGs (red) assuming $\alpha_{\rm CO} = 0.8$ M$_\odot$/(K km s^{-1} pc^2). *Right*: Distribution of log($\alpha_{6.2}$) for the 5MUSES MS galaxies. The red line corresponds to the best-fitting Gaussian profile to the data with a mean value of 1.09 and a standard deviation $\sigma = 0.30$.

in dense PDRs, PAHs may be responsible for a significant fraction of the H_2 formation at a rate comparable to that of H_2 formation on dust grains (Castellanos et al. 2018a,b). If so, a correlation between PAHs and $M_{\rm H_2}$ could thus be expected.

The CO–PAH luminosity relation is not the only piece of evidence for a potential link between $L_{6.2}$ and $M_{\rm H_2}$. In Section 3.5, we used CO-independent $M_{\rm H_2}$ estimates through the $\delta_{\rm GDR}-Z$ technique and found a linear $L_{6.2}$–$M_{\rm H_2}$ relation for normal SFGs. The relation in equation (5) can then be used to define: $M_{\rm H_2} = \alpha_{6.2} \times L_{6.2}$, where $\alpha_{6.2}$ is the parameter converting $L_{6.2}$ to $M_{\rm H_2}$. The inferred $\alpha_{6.2}$ conversion factor of our sample of MS galaxies are shown in Fig. 10 (*left*). It appears that $\alpha_{6.2}$ is independent of redshift for MS galaxies with an average value of $\langle \log(\alpha_{6.2}) \rangle = 1.09$ and a standard deviation of 0.30 (Fig. 10 *right*). An obvious caveat for the derivation of $M_{\rm H_2}$ from $L_{6.2}$, similar to the $\delta_{\rm GDR}$ and CO technique, is the dependence on metallicity which becomes challenging especially for SB systems and low-mass galaxies. For speculation, we overplot local ULIRGs in Fig. 10 (*left*) inferring their $M_{\rm H_2}$ estimates from $L'_{\rm CO}$ and assuming the commonly adopted $\alpha_{\rm CO} = 0.8$ M$_\odot$/(K km s^{-1} pc^2). Naturally, lower $\alpha_{\rm CO}$ values lead to lower $\alpha_{6.2}$ values for SB systems.

With the upcoming launch of the *James Webb Space Telescope* (*JWST*), PAH features will be detected and spatially resolved with MIRI out to $z \sim 3.5$. Our analysis suggests that PAHs can be used as a tool to infer the total amount and the spatial distribution of the molecular gas in systems that will probably be too faint to be detected by *Herschel* and thus lack any FIR photometric coverage. Since the most prominent and bright PAH feature is the one at 7.7 μm, it is worth to present its scaling relation with $M_{\rm H_2}$ as well. Repeating our analysis using $L_{7.7}$, we then find:

$$\log\left(\frac{M_{\rm H_2}}{M_\odot}\right) = \log\left(\frac{L_{7.7}}{L_\odot}\right) + (0.55 \pm 0.02) \quad (6)$$

with an intrinsic dispersion of 0.28 dex.

5 CONCLUSIONS

We have presented 24 new CO(1–0) observations of intermediate redshift ($0.03 < z < 0.30$) SFGs drawn from the 5MUSES sample that also benefits from existing *Spitzer* IRS spectroscopy and FIR photometry observations from *Spitzer* and *Herschel*. Complementing our study with literature CO, PAH, and dust observations, we investigate scaling relations between the various components of the ISM of galaxies covering a wide range of redshifts and physical conditions. We summarize our conclusions as follows:

(i) We confirm the existence of a correlation between the PAH and CO emission on global integrated scales and for the first time determine its slope and scatter in a robust statistical way. The linear and tight $L_{6.2}$–$L'_{\rm CO}$ correlation (slope of ∼1.0 and intrinsic scatter $\sigma = 0.26$ dex) is followed by the majority of galaxies at all redshifts, independent of the galaxy type.

(ii) We find evidence that on galaxy integrated scales, $L_{6.2}$ traces better the cold dust ($\lambda > 100$ μm) rather than the warm dust emission ($\lambda = 24$ μm). This is in agreement with spatially resolved observations of local galaxies. The fact that both CO and cold dust emission are tracing molecular gas, motivates us to propose that PAHs may serve as a gas tracer in SFGs.

(iii) We define a $\alpha_{6.2} = M_{\rm H_2}/L_{6.2}$ conversion factor of $2.7 \times \alpha_{\rm CO}$, where $\alpha_{\rm CO}$ is the $L'_{\rm CO}$ to $M_{\rm H_2}$ conversion factor. For normal SFGs we find $\alpha_{6.2} = 12.30$ M$_\odot$/L$_\odot$ ($\sigma = 0.30$ dex), which is consistent with $\alpha_{\rm CO} \approx 4.5$ M$_\odot$/(K km s^{-1} pc^2), typical of normal SFGs.

We conclude that $L_{6.2}$ can effectively probe the molecular gas mass in galaxies within a factor of ∼2 and propose that with the launch of *JWST*, PAHs could serve as a useful tool to trace the ISM properties in SFGs up to $z \sim 3.5$.

ACKNOWLEDGEMENTS

IC acknowledges support from Villum Fonden research grant (13160). GEM acknowledges support from the Carlsberg Foundation and a research grant (13160) from Villum Fonden. GEM, ST, CGC, and MS acknowledge support from the ERC Consolidator Grant funding scheme (project ConTExt, grant number No. 648179). This work includes observations carried with the IRAM 30 m telescope, which is supported by INSU/CNRS (France), MPG (Germany), and IGN (Spain). The Cosmic Dawn Center is funded by the Danish National Research Foundation. This research has made use of the NASA/IPAC Extragalactic Data base (NED), which is operated by the Jet Propulsion Laboratory, California Institute of Technology, under contract with the National Aeronautics and Space Administration.

REFERENCES

Akimkin V. V., Kirsanova M. S., Pavlyuchenkov Y. N., Wiebe D. S., 2015, MNRAS, 449, 440
Akimkin V. V., Kirsanova M. S., Pavlyuchenkov Y. N., Wiebe D. S., 2017, MNRAS, 469, 630
Alonso-Herrero A. et al., 2014, MNRAS, 443, 2766
Alonso-Herrero A. et al., 2016, MNRAS, 455, 563
Aravena M. et al., 2010, ApJ, 718, 177
Armus L. et al., 2007, ApJ, 656, 148
Bakes E. L. O., Tielens A. G. G. M., 1994, ApJ, 427, 822
Bendo G. J. et al., 2008, MNRAS, 389, 629
Bendo G. J. et al., 2010, MNRAS, 402, 1409
Berta S., Lutz D., Genzel R., Förster-Schreiber N. M., Tacconi L. J., 2016, A&A, 587, A73
Blitz L., Rosolowsky E., 2006, ApJ, 650, 933
Bothwell M. S. et al., 2013, MNRAS, 429, 3047
Bouché N. et al., 2007, ApJ, 671, 303
Boulanger F., Beichman C., Desert F. X., Helou G., Perault M., Ryter C., 1988, ApJ, 332, 328
Boulanger F., Falgarone E., Puget J. L., Helou G., 1990, ApJ, 364, 136
Brandl B. R. et al., 2006, ApJ, 653, 1129

Bruzual G., Charlot S., 2003, MNRAS, 344, 1000
Calzetti D. et al., 2005, ApJ, 633, 871
Calzetti D. et al., 2007, ApJ, 666, 870
Carilli C. L. et al., 2010, ApJ, 714, 1407
Casey C. M., Narayanan D., Cooray A., 2014, Phys. Rep., 541, 45
Casey C. M. et al., 2011, MNRAS, 415, 2723
Castellanos P., Candian A., Andrews H., Tielens A. G. G. M., 2018b, A&A, 616, A167
Castellanos P., Candian A., Zhen J., Linnartz H., Tielens A. G. G. M., 2018a, A&A, 616, A166
Chabrier G., 2003, PASP, 115, 763
Cherchneff I., Barker J. R., Tielens A. G. G. M., 1992, ApJ, 401, 269
Chung A., Narayanan G., Yun M. S., Heyer M., Erickson N. R., 2009, AJ, 138, 858
Churchwell E. et al., 2006, ApJ, 649, 759
Daddi E. et al., 2010a, ApJ, 713, 686
Daddi E. et al., 2010b, ApJ, 714, L118
Dale D. A. et al., 2009, ApJ, 693, 1821
Dale D. A. et al., 2012, ApJ, 745, 95
Desai V. et al., 2007, ApJ, 669, 810
Diamond-Stanic A. M., Rieke G. H., 2010, ApJ, 724, 140
Dickinson M. FIDEL Team, 2007, American Astronomical Society Meeting Abstracts. p. 822
Draine B. T., Li A., 2007, ApJ, 657, 810
Díaz-Santos T. et al., 2011, ApJ, 741, 32
Eales S. et al., 2012, ApJ, 761, 168
Elbaz D. et al., 2007, A&A, 468, 33
Elbaz D. et al., 2011, A&A, 533, A119
Engelbracht C. W., Gordon K. D., Rieke G. H., Werner M. W., Dale D. A., Latter W. B., 2005, ApJ, 628, L29
Esquej P. et al., 2014, ApJ, 780, 86
Fadda D. et al., 2006, AJ, 131, 2859
Fadda D. et al., 2010, ApJ, 719, 425
Farrah D., Afonso J., Efstathiou A., Rowan-Robinson M., Fox M., Clements D., 2003, MNRAS, 343, 585
Farrah D. et al., 2008, ApJ, 677, 957
Fazio G. G. et al., 2004, ApJS, 154, 10
Frayer D. T. et al., 2008, ApJ, 680, L21
Förster Schreiber N. M., Roussel H., Sauvage M., Charmandaris V., 2004, A&A, 419, 501
Gao Y., Solomon P. M., 2004, ApJ, 606, 271
Genzel R. et al., 1998, ApJ, 498, 579
Genzel R. et al., 2010, MNRAS, 407, 2091
Griffin M. J. et al., 2010, A&A, 518, L3
Haas M., Klaas U., Bianchi S., 2002, A&A, 385, L23
Helou G., Malhotra S., Hollenbach D., Dale D., Contursi A., 2001, ApJ, 548, L73
Helou G., Ryter C., Soifer B. T., 1991, ApJ, 376, 505
Helou G. et al., 2004, ApJS, 154, 253
Herbst E., 1991, ApJ, 366, 133
Houck J. R., Weedman D. W., Floc'h E. L., Hao L., 2007, ApJ, 671, 323
Houck J. R. et al., 2005, ApJ, 622, L105
Huang J.-S. et al., 2009, ApJ, 700, 183
Hunt L. K., Thuan T. X., Izotov Y. I., Sauvage M., 2010, ApJ, 712, 164
Hönig S. F., Kishimoto M., Gandhi P., Smette A., Asmus D., Duschl W., Polletta M., Weigelt G., 2010, A&A, 515, A23
Ivison R. J., Papadopoulos P. P., Smail I., Greve T. R., Thomson A. P., Xilouris E. M., Chapman S. C., 2011, MNRAS, 412, 1913
Jensen J. J. et al., 2017, MNRAS, 470, 3071
Jones A. G. et al., 2015, MNRAS, 448, 168
Kelly B. C., 2007, ApJ, 665, 1489
Kennicutt R. C., Jr., 1998, ARA&A, 36, 189
Kennicutt R. C., Jr. et al., 2003, PASP, 115, 928
Kim D.-C., Veilleux S., Sanders D. B., 1998, ApJ, 508, 627
Kirkpatrick A. et al., 2014, ApJ, 796, 135
Kirkpatrick A. et al., 2017, ApJ, 849, 111
Krumholz M. R., Dekel A., McKee C. F., 2012, ApJ, 745, 69
Kuno N. et al., 2007, PASJ, 59, 117
Latter W. B., 1991, ApJ, 377, 187
Laurent O., Mirabel I. F., Charmandaris V., Gallais P., Madden S. C., Sauvage M., Vigroux L., Cesarsky C., 2000, A&A, 359, 887
Lebouteiller V., Brandl B., Bernard-Salas J., Devost D., Houck J. R., 2007, ApJ, 665, 390
Leroy A. K., Walter F., Brinks E., Bigiel F., de Blok W. J. G., Madore B., Thornley M. D., 2008, AJ, 136, 2782
Leroy A. K. et al., 2011, ApJ, 737, 12
Lonsdale C. J. et al., 2003, PASP, 115, 897
Lutz D., Kunze D., Spoon H. W. W., Thornley M. D., 1998, A&A, 333, L75
Magdis G. E. et al., 2010, MNRAS, 401, 1521
Magdis G. E. et al., 2011, A&A, 534, A15
Magdis G. E. et al., 2012, ApJ, 758, L9
Magdis G. E. et al., 2013, A&A, 558, A136
Magdis G. E. et al., 2017, ApJ, 603, 93
Magnelli B. et al., 2012, A&A, 539, A155
Mannucci F., Cresci G., Maiolino R., Marconi A., Gnerucci A., 2010, MNRAS, 408, 2115
Melbourne J., Boyer M. L., 2013, ApJ, 764, 30
Menéndez-Delmestre K. et al., 2009, ApJ, 699, 667
Moorwood A. F. M., 1986, A&A, 166, 4
Mullaney J. R., Alexander D. M., Fine S., Goulding A. D., Harrison C. M., Hickox R. C., 2013, MNRAS, 433, 622
Mullaney J. R., Alexander D. M., Goulding A. D., Hickox R. C., 2011, MNRAS, 414, 1082
Murphy E. J., Chary R.-R., Alexander D. M., Dickinson M., Magnelli B., Morrison G., Pope A., Teplitz H. I., 2009, ApJ, 698, 1380
Narayanan D., Krumholz M. R., Ostriker E. C., Hernquist L., 2012, MNRAS, 421, 3127
Obreschkow D., Croton D., De Lucia G., Khochfar S., Rawlings S., 2009, ApJ, 698, 1467
Oliver S. J. et al., 2010, A&A, 518, L21
Oliver S. J. et al., 2012, MNRAS, 424, 1614
O'Dowd M. J. et al., 2009, ApJ, 705, 885
Pahre M. A., Ashby M. L. N., Fazio G. G., Willner S. P., 2004, ApJS, 154, 235
Papadopoulos P. P., van der Werf P. P., Xilouris E. M., Isaak K. G., Gao Y., Mühle S., 2012, MNRAS, 426, 2601
Peeters E., Spoon H. W. W., Tielens A. G. G. M., 2004, ApJ, 613, 986
Pereira-Santaella M., Alonso-Herrero A., Rieke G. H., Colina L., Díaz-Santos T., Smith J.-D. T., Pérez-González P. G., Engelbracht C. W., 2010, ApJS, 188, 447
Pereira-Santaella M., Rigopoulou D., Farrah D., Lebouteiller V., Li J., 2017, MNRAS, 470, 1218
Pety J., Teyssier D., Fossé D., Gerin M., Roueff E., Abergel A., Habart E., Cernicharo J., 2005, A&A, 435, 885
Pope A. et al., 2008, ApJ, 689, 127
Pope A. et al., 2013, ApJ, 772, 92
Povich M. S. et al., 2007, ApJ, 660, 346
Puget J. L., Leger A., 1989, ARA&A, 27, 161
Regan M. W. et al., 2006, ApJ, 652, 1112
Rho J., Reach W. T., Lefloch B., Fazio G. G., 2006, ApJ, 643, 965
Riechers D. A. et al., 2013, Nature, 496, 329
Riechers D. A. et al., 2014, ApJ, 786, 31
Rieke G. H. et al., 2004, ApJS, 154, 25
Rigopoulou D., Pereira-Santaella M., Magdis G. E., Cooray A., Farrah D., Marques-Chaves R., Perez-Fournon I., Riechers D., 2018, MNRAS, 473, 20
Rigopoulou D., Spoon H. W. W., Genzel R., Lutz D., Moorwood A. F. M., Tran Q. D., 1999, AJ, 118, 2625
Roche P. F., Aitken D. K., Smith C. H., Ward M. J., 1991, MNRAS, 248, 606
Roussel H., Sauvage M., Vigroux L., Bosma A., 2001, A&A, 372, 427
Rujopakarn W., Rieke G. H., Weiner B. J., Pérez-González P., Rex M., Walth G. L., Kartaltepe J. S., 2013, ApJ, 767, 73
Sajina A., Yan L., Armus L., Choi P., Fadda D., Helou G., Spoon H., 2007, ApJ, 664, 713
Sajina A. et al., 2008, ApJ, 683, 659

Salpeter E. E., 1955, ApJ, 121, 161
Sanders D. B., Scoville N. Z., Soifer B. T., 1991, ApJ, 370, 158
Sandstrom K. M., Bolatto A. D., Draine B. T., Bot C., Stanimirović S., 2010, ApJ, 715, 701
Sandstrom K. M. et al., 2012, ApJ, 744, 20
Sandstrom K. M. et al., 2013, ApJ, 777, 5
Sargent M.T. et al., 2014, ApJ, 793, 19
Schmidt M., 1959, ApJ, 129, 243
Schreiber C. et al., 2015, A&A, 575, A74
Scoville N. et al., 2017, ApJ, 837, 150
Sellgren K., 1984, ApJ, 277, 623
Shipley H. V., Papovich C., Rieke G. H., Brown M. J. I., Moustakas J., 2016, ApJ, 818, 60
Shipley H. V., Papovich C., Rieke G. H., Dey A., Jannuzi B. T., Moustakas J., Weiner B., 2013, ApJ, 769, 75
Shi Y., Helou G., Yan L., Armus L., Wu Y., Papovich C., Stierwalt S., 2011, ApJ, 733, 87
Silverman J. D. et al., 2015, ApJ, 812, L23
Smith J. D. T. et al., 2007, ApJ, 656, 770
Solomon P. M., Downes D., Radford S. J. E., Barrett J. W., 1997, ApJ , 478, 144
Solomon P. M., Rivolo A. R., Barrett J., Yahil A., 1987, ApJ, 319, 730
Solomon P. M., Vanden Bout P. A., 2005, ARA&A, 43, 677
Speagle J. S., Steinhardt C. L., Capak P. L., Silverman J. D., 2014, ApJS, 214, 15
Spoon H. W. W., Marshall J. A., Houck J. R., Elitzur M., Hao L., Armus L., Brandl B. R., Charmandaris V., 2007, ApJ, 654, L49
Tacconi L. J. et al., 2006, ApJ, 640, 228
Tacconi L. J. et al., 2008, ApJ, 680, 246
Tacconi L. J. et al., 2018, ApJ, 853, 179
Thilker D. A. et al., 2007, ApJS, 173, 572
Tielens A. G. G. M., 2008, ARA&A, 46, 289
Tielens A. G. G. M., Seab C. G., Hollenbach D. J., McKee C. F., 1987, ApJ, 319, L109
Valiante E., Lutz D., Sturm E., Genzel R., Tacconi L. J., Lehnert M. D., Baker A. J., 2007, ApJ, 660, 1060
Veilleux S. et al., 2009, ApJS , 182, 628
Weedman D. W. et al., 2005, ApJ, 633, 706
Wilson C. D. et al., 2012, MNRAS, 424, 3050
Wu Y. et al., 2010, ApJ, 723, 895
Yan L. et al., 2007, ApJ, 658, 778
Yan L. et al., 2010, ApJ, 714, 100

SUPPORTING INFORMATION

Supplementary data are available at *MNRAS* online.

Table 3. General properties of the 5MUSES sample.
Table 4. Galaxies from the literature with PAH, IR, and/or CO emission.

Please note: Oxford University Press is not responsible for the content or functionality of any supporting materials supplied by the authors. Any queries (other than missing material) should be directed to the corresponding author for the article.

This paper has been typeset from a TEX/LATEX file prepared by the author.